APHELION CLOUD FORMATION AND SWISS CHEESE SUBLIMATION: MARTIAN ATMOSPHERIC WATER VAPOUR PROCESSES

ALEX C. INNANEN

A THESIS SUBMITTED TO
THE FACULTY OF GRADUATE STUDIES
IN PARTIAL FULFILLMENT OF THE REQUIREMENTS
FOR THE DEGREE OF

MASTER OF SCIENCE

GRADUATE PROGRAM IN EARTH AND SPACE SCIENCE
YORK UNIVERSITY
TORONTO, ONTARIO

November 2021

Abstract

The behaviour of atmospheric water vapour was studied at two points in the Martian water cycle: the formation of the Aphelion Cloud Belt (ACB) in Northern spring and summer and the sublimation of the south polar cap in Northern autumn and winter (Southern spring and summer). We derived an average phase function for ACB water-ice clouds for Mars year (MY) 35, and compared it with the previously derived MY 34 phase function to determine if the global dust storm of MY 34 had any impact on the formation of Aphelion clouds. We found that there was little difference in the two phase functions, and likely the dominant ice crystal habit was not effected by the global dust storm. We compared our derived phase function to four previously derived Martian water-ice cloud phase functions and seven modeled water-ice crystal phase functions, and found little agreement with our phase function. We also derived morning and afternoon phase functions for the MY 35 ACB season, and saw little difference between the two.

We mapped Swiss cheese features on the south polar residual cap (SPRC), and retrieved surface temperature values of Swiss cheese terrain sites from the Mars Climate Sounder (MCS) in order to determine water-ice temperatures within Swiss cheese features. We determined the current water vapour contribution from Swiss cheese features exposing water ice to be negligible compared to the amount of southern summer water vapour produced by other processes. We also determined the area of exposed water ice needed to sublimate 30 pr μm of water vapour from Swiss cheese features to be 78 678 km^2 at 173 K, and that it was impossible to sublimate this amount of water vapour from the SPRC at lower temperatures.

Table of Contents

List of Tables

List of Figures

Chapter 1

Introduction

1.1 An Introduction to Martian Atmospheric Water Vapour

While the Martian atmosphere is colder, thinner and drier than Earth's, the two atmospheres do bear resemblance, and understanding one can enhance our understanding of the other. Mars' rotational period (*Sol*) is only 39.6 minutes longer than that of Earth, and its axial tilt of 25.19° gives rise to seasons like those on Earth. The major constituents of the Martian atmosphere are CO_2 (95.1%), N_2 (2.59%), Ar (1.94%) and O_2 (0.16%), as well as trace amounts of other gasses, such as water vapour (Williams, 2020). Additionally, dust suspended in the atmosphere can have significant impacts on the thermal structure and dynamics of that atmosphere (Kahre et al, 2017).

The study of the Martian atmosphere dates back to William Herschel, who suggested Mars had a 'considerable but moderate atmosphere', and who also observed the seasonal retreat and growth of the polar ice caps (Herschel, 1784). The 20th century saw further telescopic observations, as well as missions to Mars itself in the form of orbiters and landers. The first remote detection of water vapour was in 1963 by Spinrad et al, who estimated a column abundance between 5 and 10 precipitable microns (*pr μm)* of water vapour above the Martian poles (Spinrad et al, 1963). The amount of atmospheric water vapour changes throughout the year, following a cycle of autumn-winter deposition and spring-summer sublimation from the polar ice caps. During the northern summer (southern winter), water vapour sublimated from the north polar cap is transported southwards, while in the northern winter (southern summer), the opposite is true, with water vapour sublimated from the south polar cap being transported northwards. The northern polar cap is a far greater source of water than the southern, and it is only during the northern summer transport that we see the formation of water-ice clouds, notably the Aphelion Cloud Belt (described in more detail in Section 1.3). Additionally, the eccentricity of Mars'

orbit means that south polar summers are on the order of 20 K warmer at their peak than those of the north pole (Montmessin et al, 2017). The global annually averaged column abundance of water vapour is 10 pr µm, with a Northern hemisphere peak of about 60-70 pr µm and a Southern hemisphere peak of about 20 pr µm (Trokhimovskiy et al, 2015). Figure 1.1 shows the variation in water vapour abundance at different latitudes from a solar longitude (L_s) of 90° in Mars Year (MY) 24 to L_s 150° in MY 25.

Solar longitude is used to indicate season on Mars, with L_s=0° being the vernal equinox, the start of northern spring or southern autumn, and the start of a new Mars year. The conventional numbering system of Mars years established by Clancy et al (2000) gives L_s=0° of MY 1 as April 11, 1955. These timekeeping conventions are used throughout the thesis.

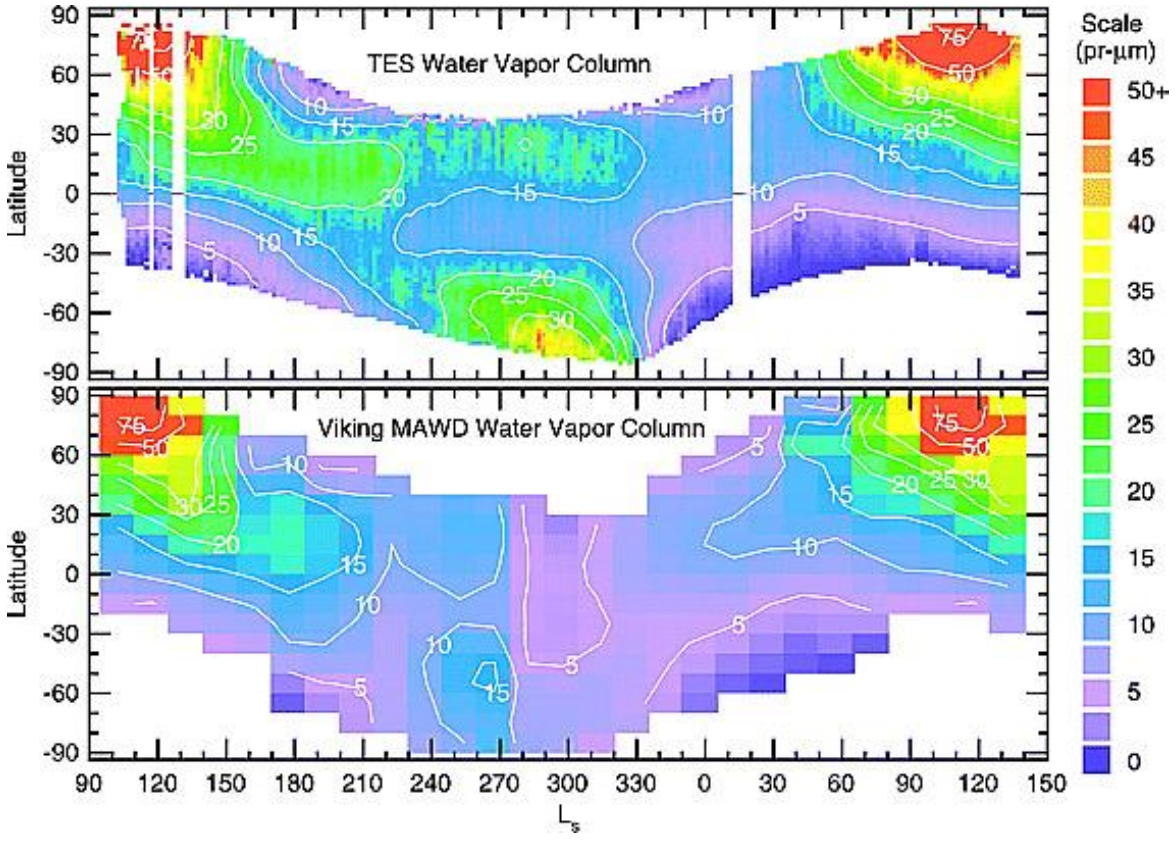

Figure 1.1: Water vapour column abundance measured by the Thermal Emission Spectrometer (TES) aboard the Mars Global Surveyor (top) and the Mars Atmospheric Water Detector (MAWD) aboard Viking (bottom) during MY 24-25 as a function of Latitude and L_s. The difference in peak water vapour

between northern and southern hemispheres can be seen, with northern hemisphere peaks around L_s=120° and southern hemisphere peaks around L_s=270°, as well as the cycle of water vapour abundance (Smith, 2002).

A significant departure from this seasonal cycle in water vapour abundance is the 1969 earth-based telescopic observation of an unusually high amount of water vapour (45-50 pr µm) above the south pole during southern summer (Barker et al, 1970). This amount of water vapour in the southern hemisphere has not been seen since, and there is currently no definitive explanation for this observation.

1.2 Global Dust Storms

The Martian dusty season spans from about L_s=135-360° and is characterised by higher dust loading of the atmosphere and the formation of local, regional and global dust storms (Kahre et al, 2017). Global dust storms (GDS) occur every few years, with the most recent three occurring in MYs 25, 28 and 34.

GDSs tend to begin in the southern hemisphere near perihelion (L_s=250°) although they have also been observed earlier and later in the dusty season (Wokenberg et al, 2020). They can have a variety of impacts on Martian meteorology, with greater dust loading impacting atmospheric circulation (Cantor, 2007). They can also impact surface albedo on large scales, brightening in some regions and darkening in others due to dust deposition or erosion of already existing dust deposits by the storm. It can take up to one Martian year for surface albedo to return to its typical levels in some cases. Long term changes in albedo can impact the planet's temperature so that an average albedo increase of 1% would lead to a global daytime surface temperature decrease of 1 K (Cantor, 2007). Following the MY 25 GDS, below average daytime atmospheric and surface temperatures persisted for an entire Mars year (Smith, 2004).

GDSs can also impact the transport of water vapour. During the storms, water vapour abundance increases in the middle atmosphere as the hygropause ascends (Heavens et al, 2018; Aoki et al, 2019). Figure 1.2 shows the vertical distribution of water vapour before, during, and after the MY 28 GDS,

showing the ascent of the hygropause to around 80 km, and the gradual return to more typical values following the GDS. Additionally, thermal tides tend to be stronger during GDSs due to high levels of atmospheric dust (Guzewich et al, 2014).

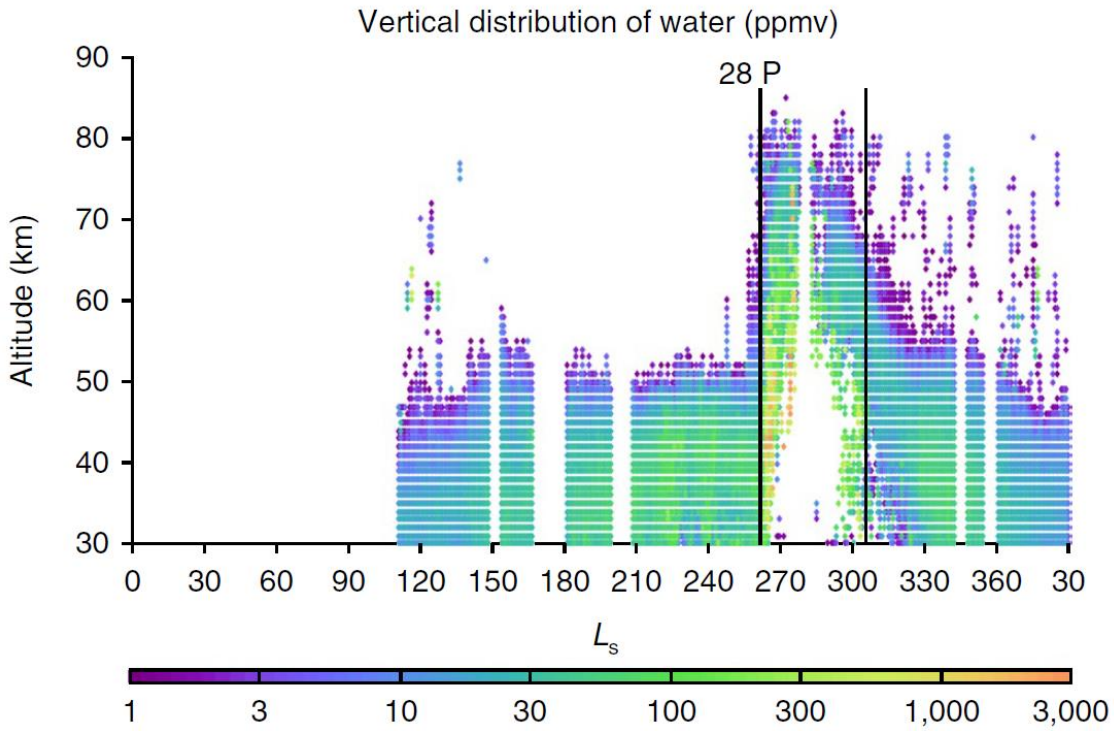

Figure 1.2: The increase in altitude of the hygropause during the MY 28 GDS (indicated by 28 P) as well as increase in water vapour content in ppmv (Heavens et al, 2018).

The MY 34 GDS began to form around L_s=188° around Acidalia and Utopia Planitia. It was labelled a planet encircling event by L_s=193°, and returned to typical seasonal levels by L_s=250° (Guzewich et al, 2019). The storm was observed from orbit as well as from the planet's surface by The Mars Science Laboratory (MSL). MSL saw increased dust opacity, with a peak optical depth of 8.5, and a minimum horizontal extinction of 2.7 km (defined as the distance to the furthest discernable object) (Guzewich et al, 2019). Figure 1.3 shows the evolving line of sight images during the storm.

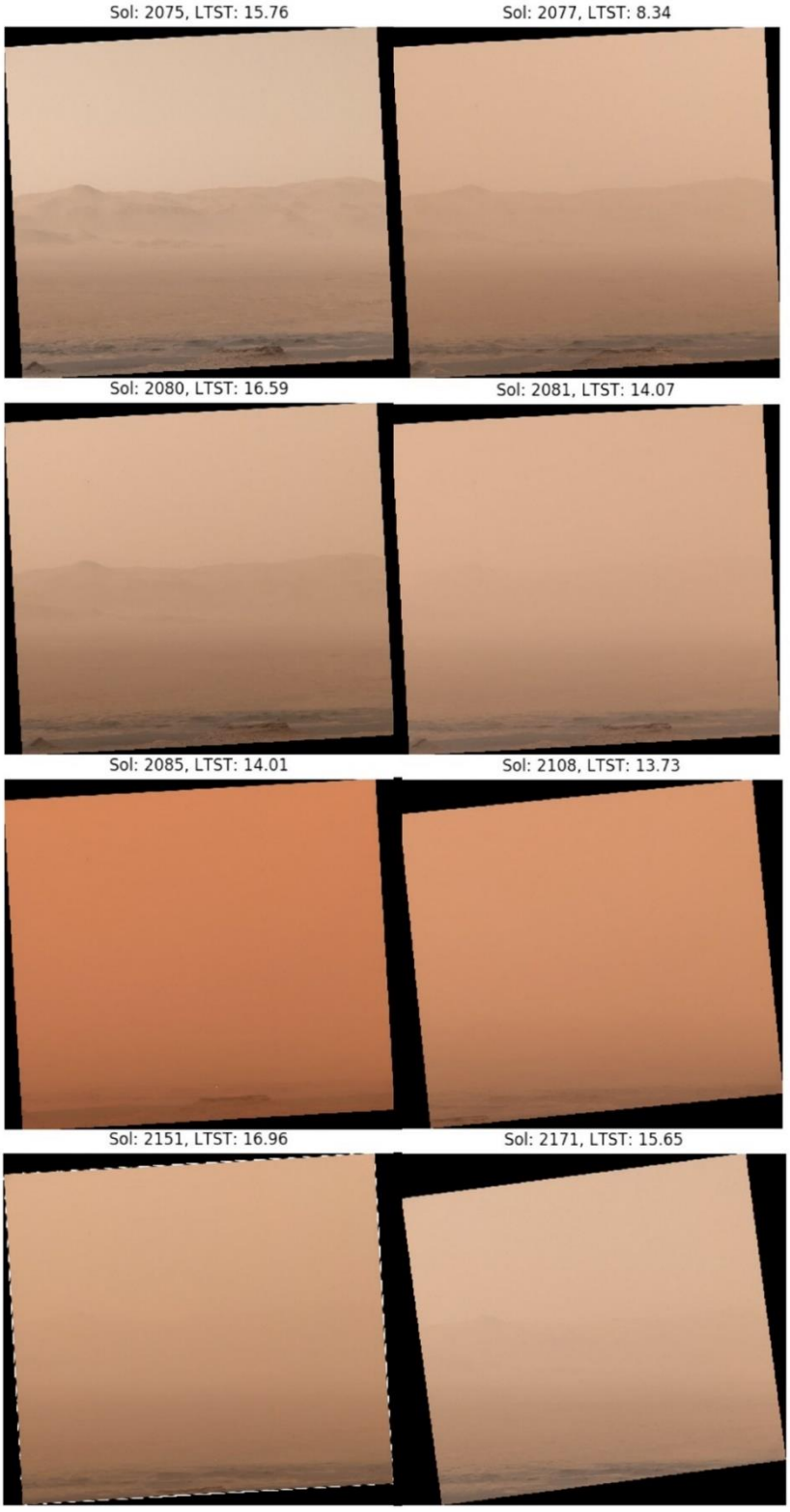

Figure 1.3: MastCam images showing deminishing line of sight extinction pointing at the crater rim during the MY 34 Global Dust Storm. The MSL sol number and local true solar time (LTST) are indicated (Fig.2 in Guzewich et al, 2019).

The Rover Environmental Monitoring Station (REMS) aboard MSL also measured pressure, air and ground temperature, water vapour abundance and UV radiation during the GDS, and saw a decrease in relative humidity and surface solar flux as well as diurnal temperature variation. Additionally, the semidiurnal pressure variation reached the highest levels seen on Mars (Guzewich et al, 2019).

Other effects of the MY 34 GDS included an increase in dust aerosol size (Lemmon et al, 2019), increased middle atmosphere water vapour (Aoki et al, 2019) and the formation of water-ice clouds that were atypical for the season (Stcherbinine et al, 2020).

1.3 Mars Water-Ice Clouds and the Aphelion Cloud Belt

Martian clouds have been studied from Earth, from orbit, and more recently, from the surface of Mars itself. They tend to be optically thin, and occur only under certain conditions, and thus were not thought to have a significant impact on the Martian climate (Montmessin et al, 2004). Studies from the 1990s and beyond have shown that this is not the case – the presence of water-ice clouds can impact the Martian water cycle, atmospheric chemistry, and radiative transfer within the atmosphere (Clancy et al, 2017). Mars water-ice clouds vary on both seasonal and diurnal timescales with certain cloud features repeating yearly such as the aphelion cloud belt and polar hood clouds. Additionally, large daytime variations in temperature can lead to changes in cloud properties over the course of a single sol (Madeleine et al, 2012).

The Aphelion Cloud Belt (ACB) is the name given to water-ice clouds that form around Mars' Aphelion (Ls=71°) from about 10°S to 30°N (Wolff et al, 1999) (Figure 1.4). The ACB season is due to the significant eccentricity of Mars' orbit (0.0935) which places Mars around 20% further from the sun at aphelion as compared to perihelion. As Mars reaches aphelion, the lower 50 km of the atmosphere cools, accompanied by an increase in water-ice clouds and a decrease in dust lofting (Clancy et al, 1996). It is

likely that the aphelion cloud belt is responsible for the asymmetry in seasonal water vapour between the northern and southern hemispheres, interrupting the flow of water vapour from the north to south in northern spring and summer through the formation of water-ice clouds (Wolff et al, 1999).

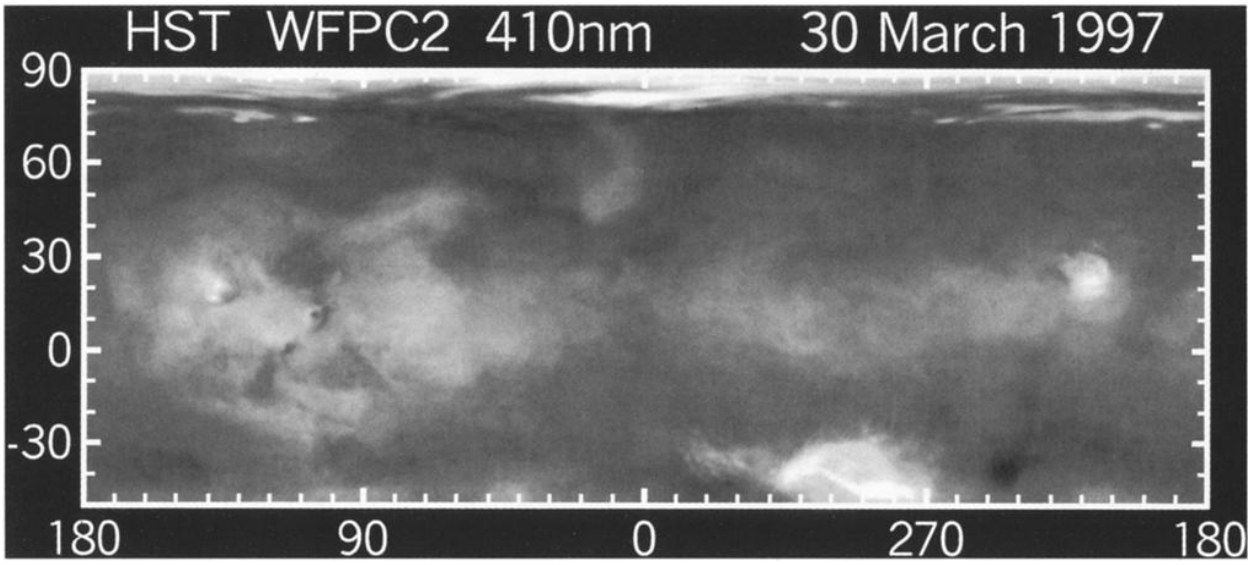

Figure 1.4: The Aphelion Cloud Belt imaged by the Hubble Space Telescope. Bright clouds are visible around near the equator, making up the ACB. Cloud formation can be seen elsewhere, but are not part of the ACB. (Malin et al, 2001)

The ACB season tends to have low interannual variability (Wolff et al, 2019), except during years with significant regional and global dust storms that can warm the atmosphere by tens of Kelvin (Cantor, 2007). Such storms can impact the length of the ACB season, such as the early disappearance of ACB clouds in MY 25 due to the formation of a GDS (Benson et al, 2003), and the later formation of the MY 29 ACB, following the MY 28 GDS (Giuranna et al, 2019). Additionally, Wolff et al (2019) saw an increase in cloud optical depth in the years bracketed by two GDSs in MY 28 and MY 34 (figure 1.5). The optically thinner water-ice clouds of MY 29 were also reported by Mateshvili et al (2009).

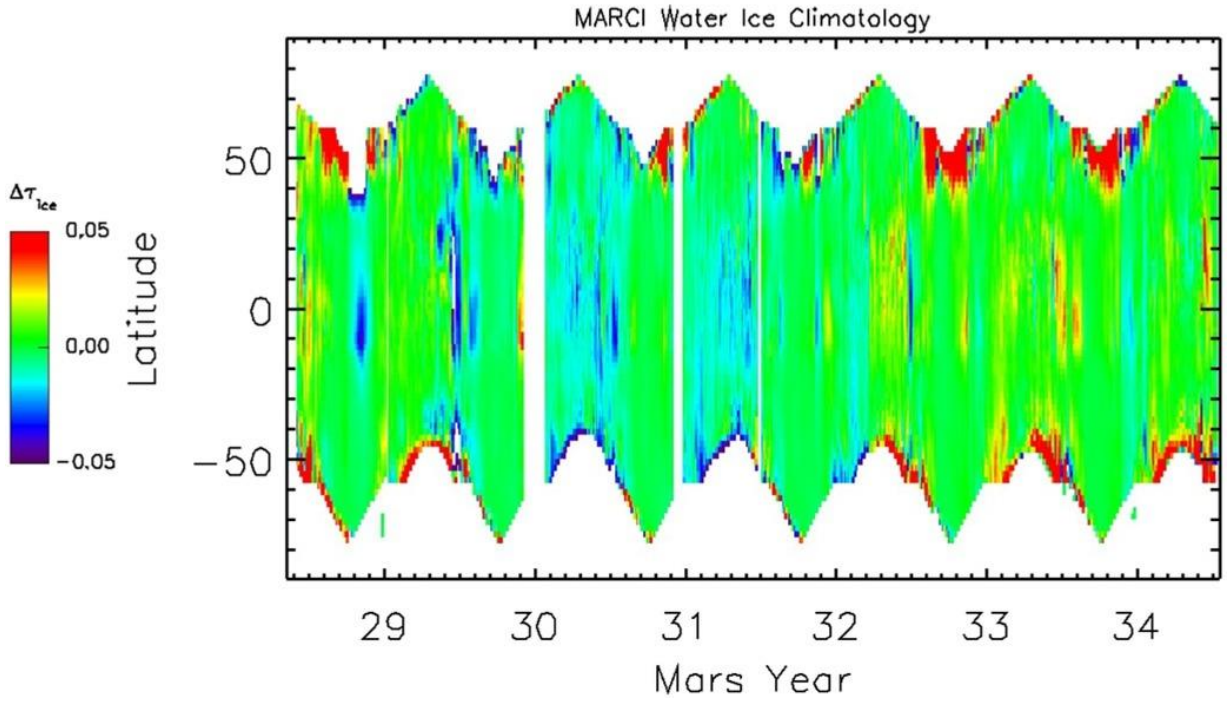

Figure 1.5: Interannual variability in water-ice optical depth, shown by subtracting the multi-year average. Negative $\Delta\tau_{ice}$ values (green-blue) represent optically thinner clouds than average, while positive $\Delta\tau_{ice}$ values (green-red) represent optically thicker clouds than average. The general trend of increasing optical depth from MY 29-34 can be seen. (Wolff et al, 2019)

ACB clouds exhibit greater diurnal than interannual variation, although diurnal trends have been studied less extensively than seasonal or interannual ones. The most cloud activity tends to occur in the mornings and afternoons, decreasing around noon. Cooler overnight temperatures allow the formation of water-ice clouds, which dissipate as temperatures rise towards noon. These rising temperatures, however, allow enhanced convection to lift dust, which acts as condensation nuclei for water vapour lifted to the saturation level (Tamppari et al, 2003). In the area of Gale Crater, Kloos et al (2018) found that there is greater cloud activity in the mornings during the ACB, and that the morning clouds had a greater optical thickness than the afternoon ones. Additionally, dividing the aphelion season into early and late seasons showed that this trend of greater morning opacity holds, but the earlier part of the season had more optically thick clouds overall in both the mornings and afternoons (Kloos et al, 2018).

Morning clouds are also more likely to form at altitudes above 35 km, while afternoon clouds have a higher likelihood between 20 and 30 km (Campbell et al, 2020).

1.4 Mars Science Laboratory Cloud Observations and Martian Scattering Phase Functions

The Mars Science Laboratory (MSL, Curiosity) has been active in Gale Crater (4.5°S, 137.4°E) since its landing in August of 2012. The main goals of the rover are to assess the habitability and past environment of the region through studying the geology and climate of Gale Crater (Grotzinger et al, 2012). In order to accomplish these goals, the rover has 10 instruments, including four scientific cameras, and navigation and hazard engineering cameras, which can also be used for scientific data collection. For instance, the rover acquires cloud movies using its navigation cameras (NavCams), two sets of cameras mounted on MSL's remote sensing mast (RSM) (shown in figure 1.6) which have a field of view of 45°x45°. The RSM is able to rotate 360° in azimuth and 178° in elevation (Maki et al, 2012). Of interest to this work are the NavCams' cloud movies.

Simple single-pointing, 8 frame movies have been taken every few sols since the beginning of MSL's mission using the NavCams. These are known as Zenith and Suprahorizon movies (ZM, SHM) and point directly overhead and just above the horizon, respectively (Moores et al 2015; Kloos et al 2018). The movies have been analysed to show morphology, optical depth, spacing (Moores et al 2015; Kloos et al 2018), altitude (Campbell et al 2019), wind direction, and angular velocity (Campbell et al, 2021).

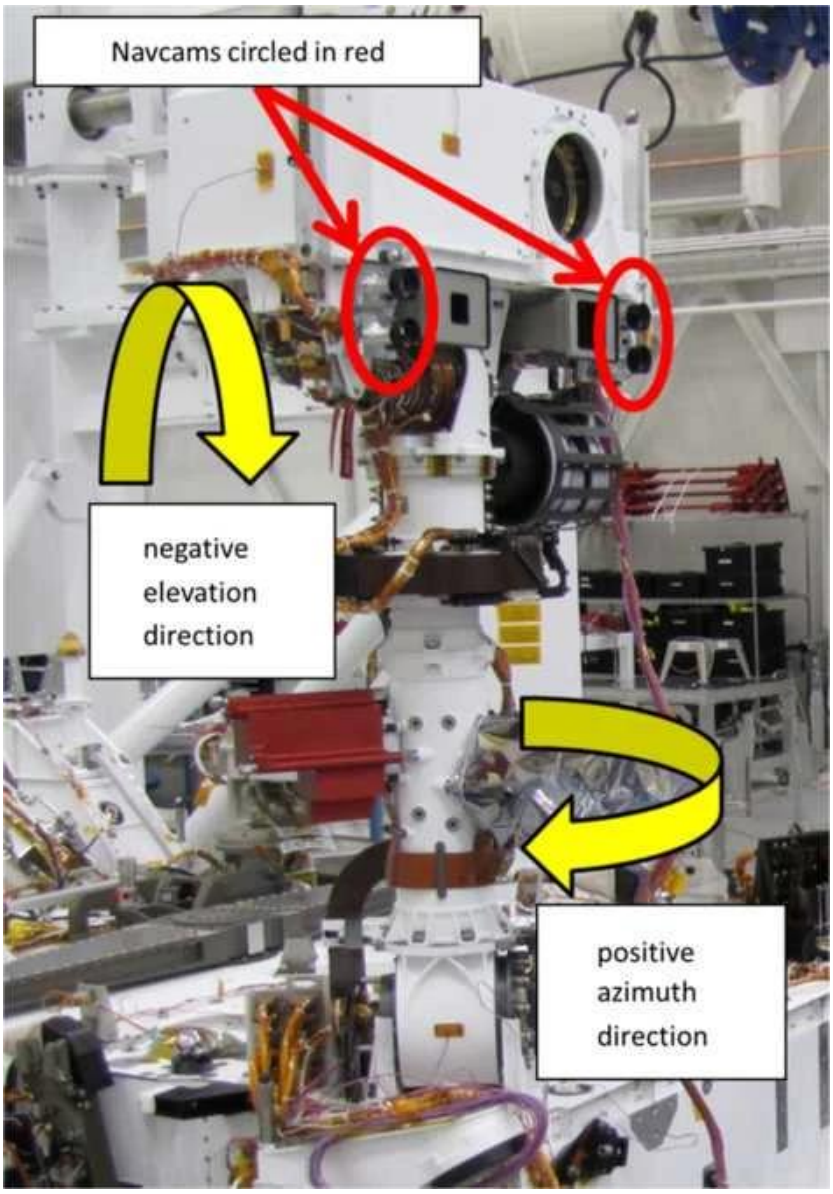

Figure 1.6: The remote sensing mast (RSM) of MSL with NavCams indicated (Fig. 3 in Maki et al, 2012).

In MY 34, a new NavCam cloud observation was instituted in order to extend the work of Kloos et al (2016). The phase function sky survey (PFSS), consists of 9 movies of three frames each at 9 different pointings forming a dome around the rover (Figure 1.7). It allows a greater range of scattering angles to be observed to characterise the single scattering phase function of water-ice clouds during the ACB season and to constrain ice crystal geometries (Cooper et al, 2019).

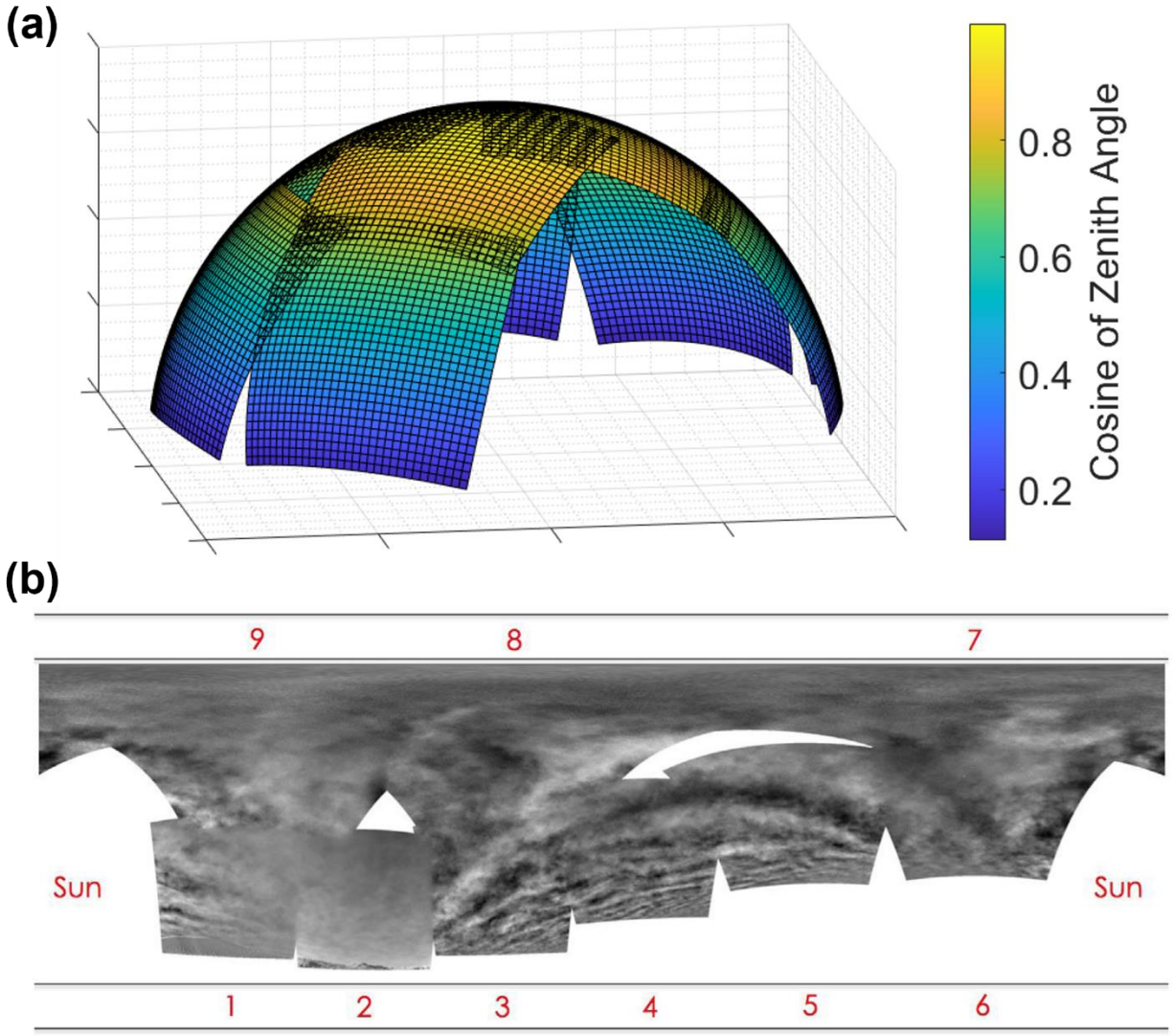

Figure 1.7: (a) Projection of PFSS pointings, with the rover at the centre. (b) A composite of the 9 pointings of the PFSS taken on Sol 1924 at 07:05 local true solar time (LTST) (Cooper et al, 2019). The gap in coverage avoids pointing at the sun.

The PFSS observation has a preferred cadence of one observation per week during the ACB season (about L_s=40° to L_s=150°), alternating between morning and afternoon observations. There is a 2.5 hour keep-out around local noon, in order to prevent the pointing optics too close to the sun, so that the cameras do not become oversaturated. The morning and afternoon observations also include a gap in their coverage (as seen in Figure 1.6) located for this purpose.

Prior to Cooper et al (2019), there have been a number of attempts to construct the phase functions of Martian water-ice clouds. Clancy & Lee (1991) and Clancy et al (2003) analysed emission phase function (EPF) observations taken from the Viking orbiter infrared thermal mapper (IRTM) and the Thermal Emission Spectrometer (TES) onboard the Mars Global Surveyor (MGS), respectively, in order to study Mars aerosol properties. While the Viking data dealt with polar and mid-latitude clouds (Clancy & Lee, 1991), the TES observations covered ACB clouds from 45°N to 45°S, which were divided into two types. Type 1 water-ice clouds had a smaller particle effective radius (1-2 μm) and were more prominent in the southern hemisphere, while Type 2 had a larger particle effective radius (3-4 μm) and were more prominent in the northern hemisphere. The scattering properties of these two cloud types indicate they likely have different water-ice crystal geometries (Clancy et al, 2003). The modeled scattering phase functions were also compared with previously derived dust phase functions (Figure 1.8).

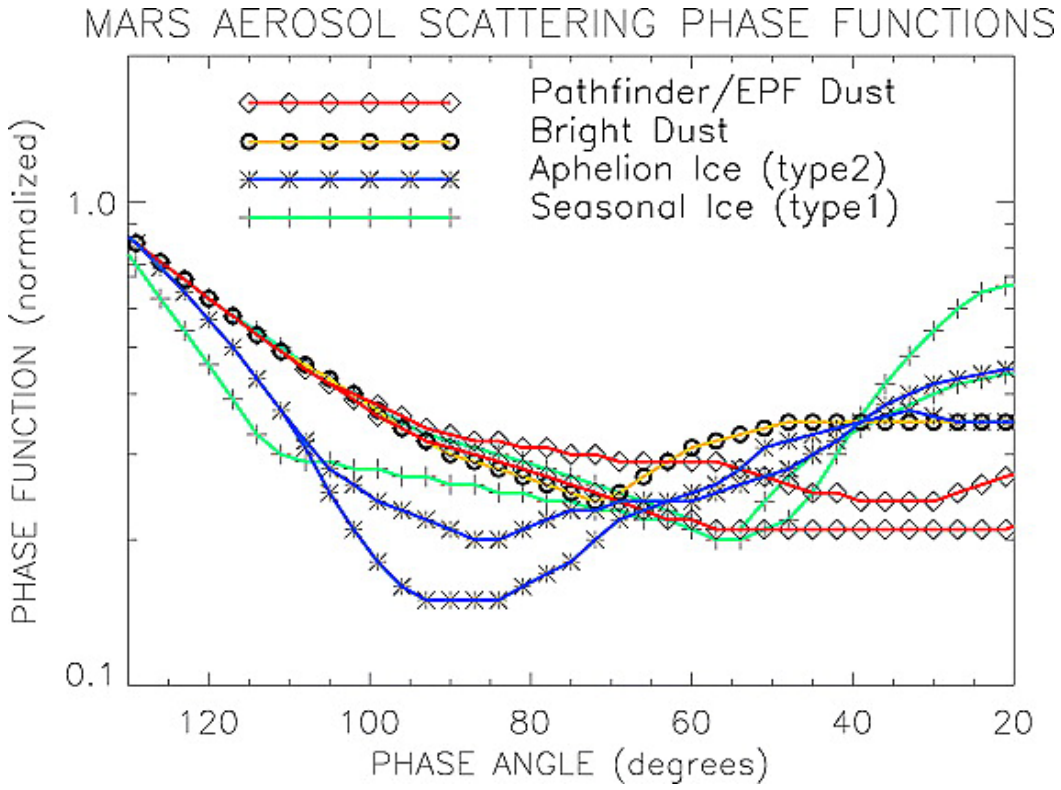

Figure 1.8: Comparison of two types of aphelion water-ice cloud scattering phase functions, from TES EPF observations over L_s=0-360° and latitude 45°S-45°N, with dust scattering phase functions from Pathfinder and Viking IRTM (Clancy et al, 2003).

Kloos et al (2016) attempted to constrain the scattering phase function of Martian clouds using 12 ZM and 8 SHM measurements over an L_s range of 6.8°-168° and scattering angles from 70° to 115°. The value of the phase function was assumed to be a lower bound (black line in Figure 1.9), due to the uncertainty involved in measuring the radiance of the cloud, also assumed to be a lower limit (a further explanation of this is in Section 2.1). The upper limit in Figure 1.9 (gold line) is taken from Figure 1 in Chepfer et al (2002) and represents the upper limit of the phase function for the 14 different ice crystal shapes in that figure.

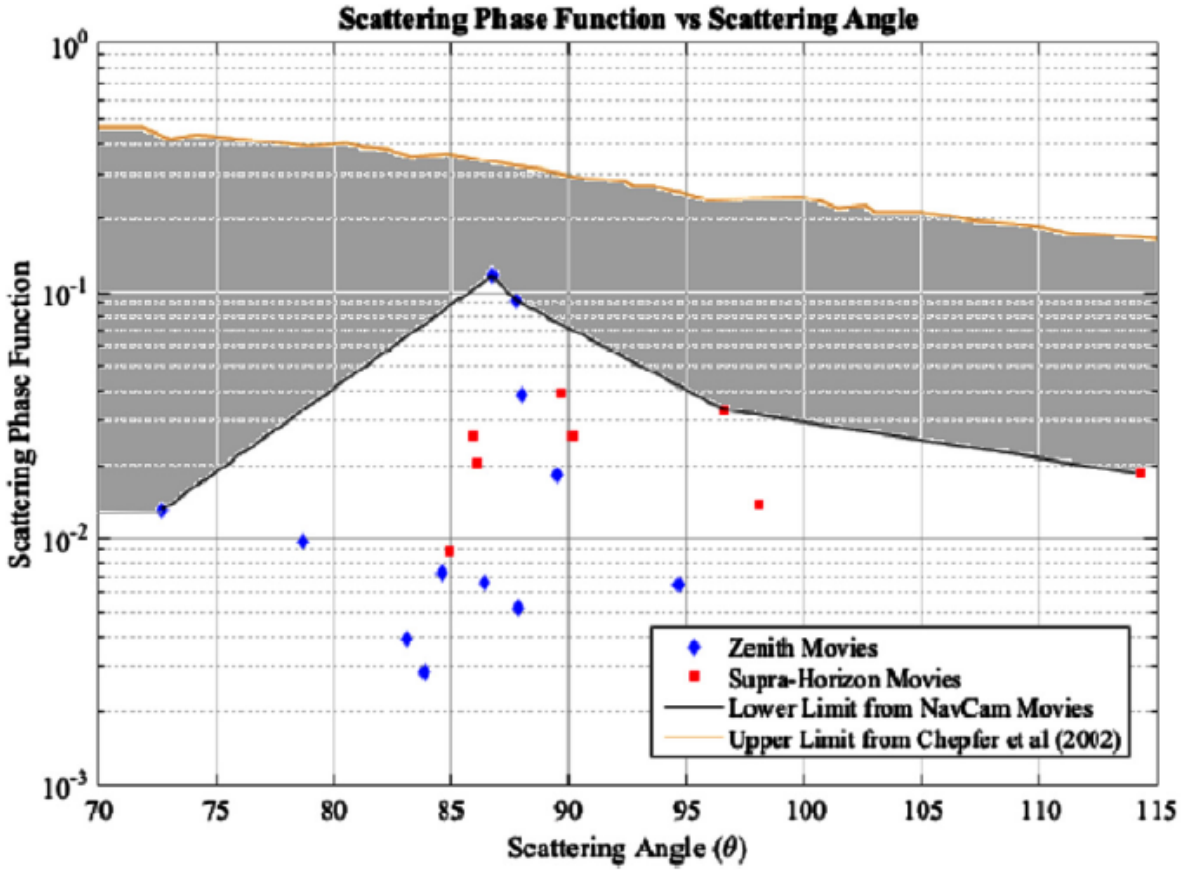

Figure 1.9: Figure 10 from Kloos et al, 2016. Scattering phase function lower (black line) and upper limits (gold line) taken from ZM and SHM measurements and Chepfer et al (2002) modeled water-ice crystal phase functions respectively. The shaded region between the two phase functions is the range used for Martian clouds observed in Kloos et al (2016).

Cooper et al (2019) was able to create a mean phase function for MY 34 from 35 PFSS observations, over scattering angles 18.3° to 152.61°, shown in figure 1.10, in order to further constrain the dominant scattering properties of Martian ACB clouds. The phase function was also compared with seven modeled water-ice crystal geometries (Figure 1.11) and three previously derived Mars water-ice cloud phase functions from Viking (Clancy & Lee, 1991) and TES (Clancy et al, 2003).

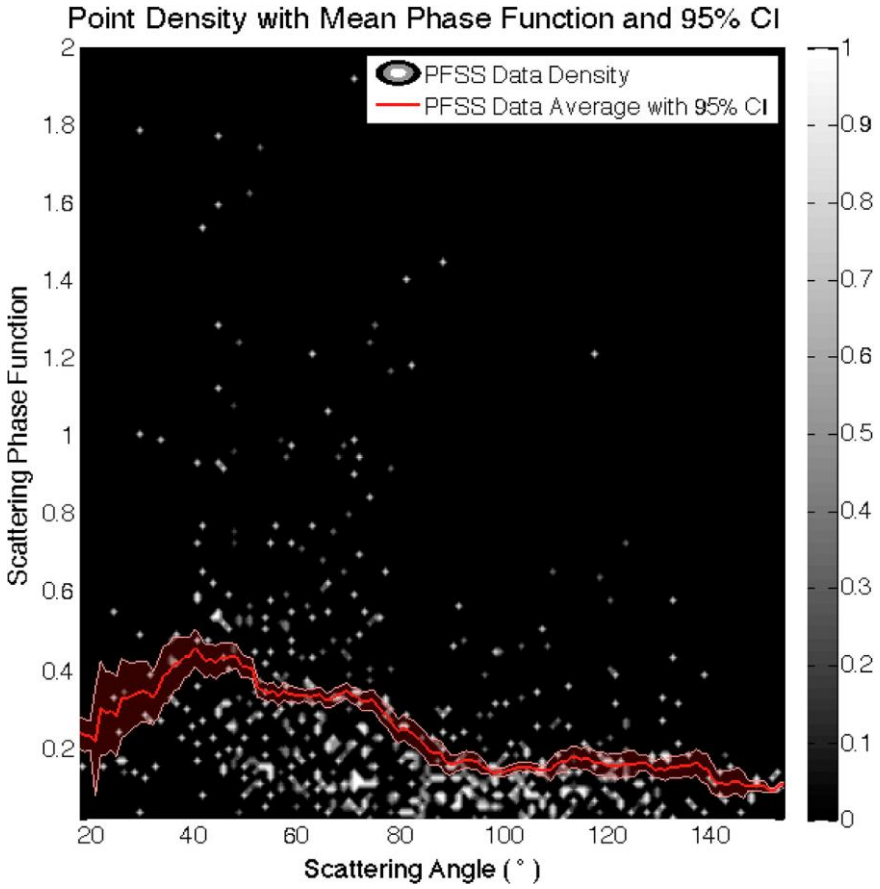

Figure 1.10: The mean curve of the derived MY 34 phase function displayed over the point density with shaded 95% confidence interval error bars (Figure 6 in Cooper et al 2019)

Cooper et al (2019) found a preference for aggregates, hexagonal solid columns, hollow columns, plates and bullet rosettes in ACB clouds, a similar makeup to terrestrial cirrus clouds. Additionally, the presence of possible local maxima near 22° and 46° could be indicative of scattering phenomena associated with terrestrial cirrus water-ice clouds (Cooper et al, 2019).

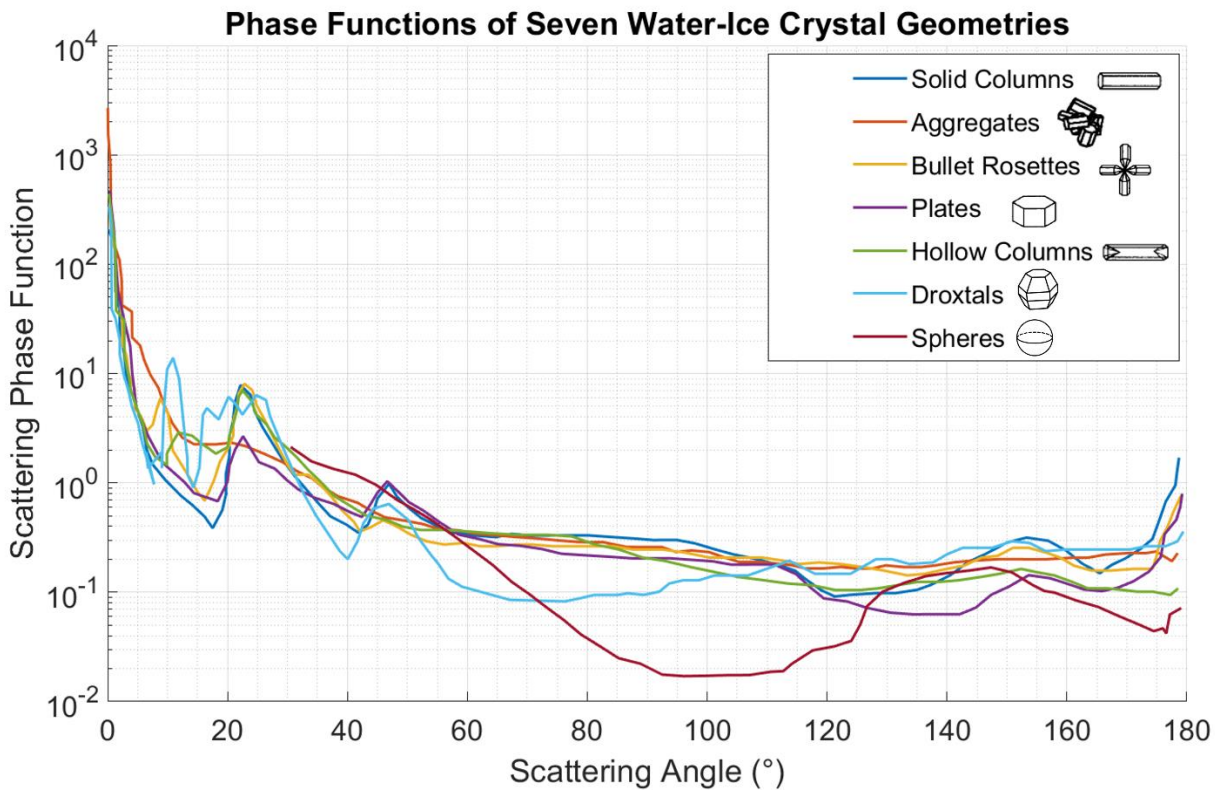

Figure 1.11: Scattering phase functions of seven modeled randomly oriented water-ice crystal geometries. Solid columns, aggregates, bullet rosettes, plates, hollow columns and spheres are modeled by Yang & Liou (1996) and droxtals are modeled by Yang et al (2010). All phase functions have an increase in magnitude in the forward scattering direction (near 0°) and a small increase in the backscattering direction (near 180°).

1.5 The Martian South Polar Residual Cap and its Impact on Atmospheric Water Vapour

The south polar deposits of Mars consist of a seasonal CO_2 ice cap, which forms during southern fall and winter and retreats in southern spring and summer; a stable, residual CO_2 ice cap (the South Polar Residual Cap, SPRC); and the underlying but more spatially extensive dusty water-ice south polar layered deposits (SPLD). The SPRC is only a few metres thick and contains a variety of morphological features and areas of exposed SPLD (Byrne, 2009 and references therein). SPRC features include long, asymmetric, parallel depressions known as 'fingerprint terrain', raised mesas, and smaller curl, heart-

shaped, and quasi-circular depressions known as 'Swiss cheese' features (Thomas et al, 2009), as shown in Figure 1.12.

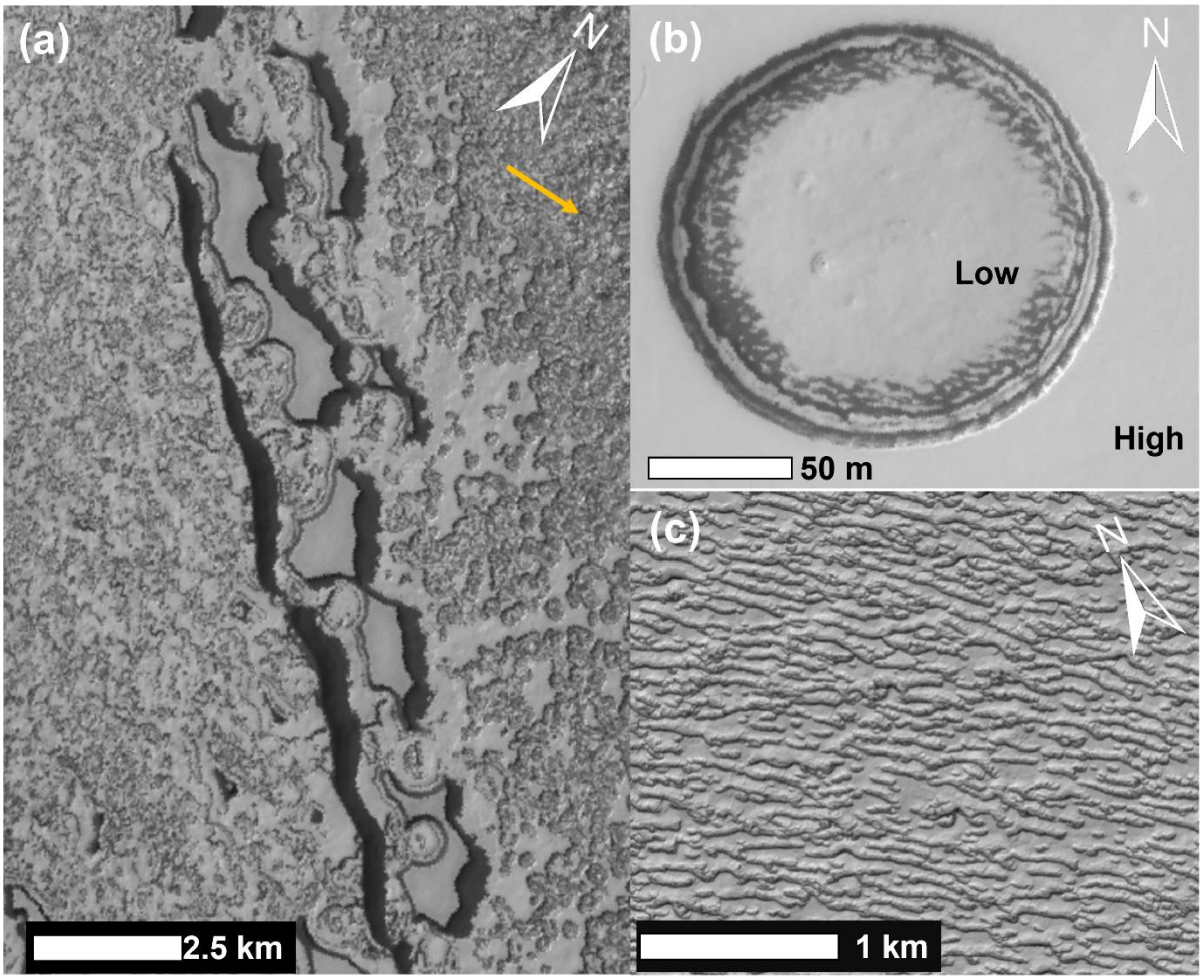

Figure 1.12: (a) raised mesas (smooth features) surrounded by newer, eroded material, centred at 86.8°S, 16.4°E. (Murray Lab CTX Mosaic, Dickson et al 2018). Yellow arrow indicates direction of sunlight (b) quasi-circular 'Swiss cheese' feature centred at 86.8°S, 110.7°W. (HiRISE image PSP_005349_0930). (c) linear 'fingerprint' terrain centred at 86.6°S, 24.17°W. (Murray Lab CTX Mosaic, Dickson et al 2018).

Figure 1.13 shows the extent of these features on the SPRC. The SPRC thickness ranges from about 10-14 m to ~1 m in younger areas, which comprise most of the SPRC (Thomas et al, 2009). Below the SPRC is a massive CO_2 ice deposit as detected in radar under a water ice capping unit (Philips et al, 2011). Also

present are large, spiral troughs (dark features in Figure 1.13) which are present on both the north and south polar caps.

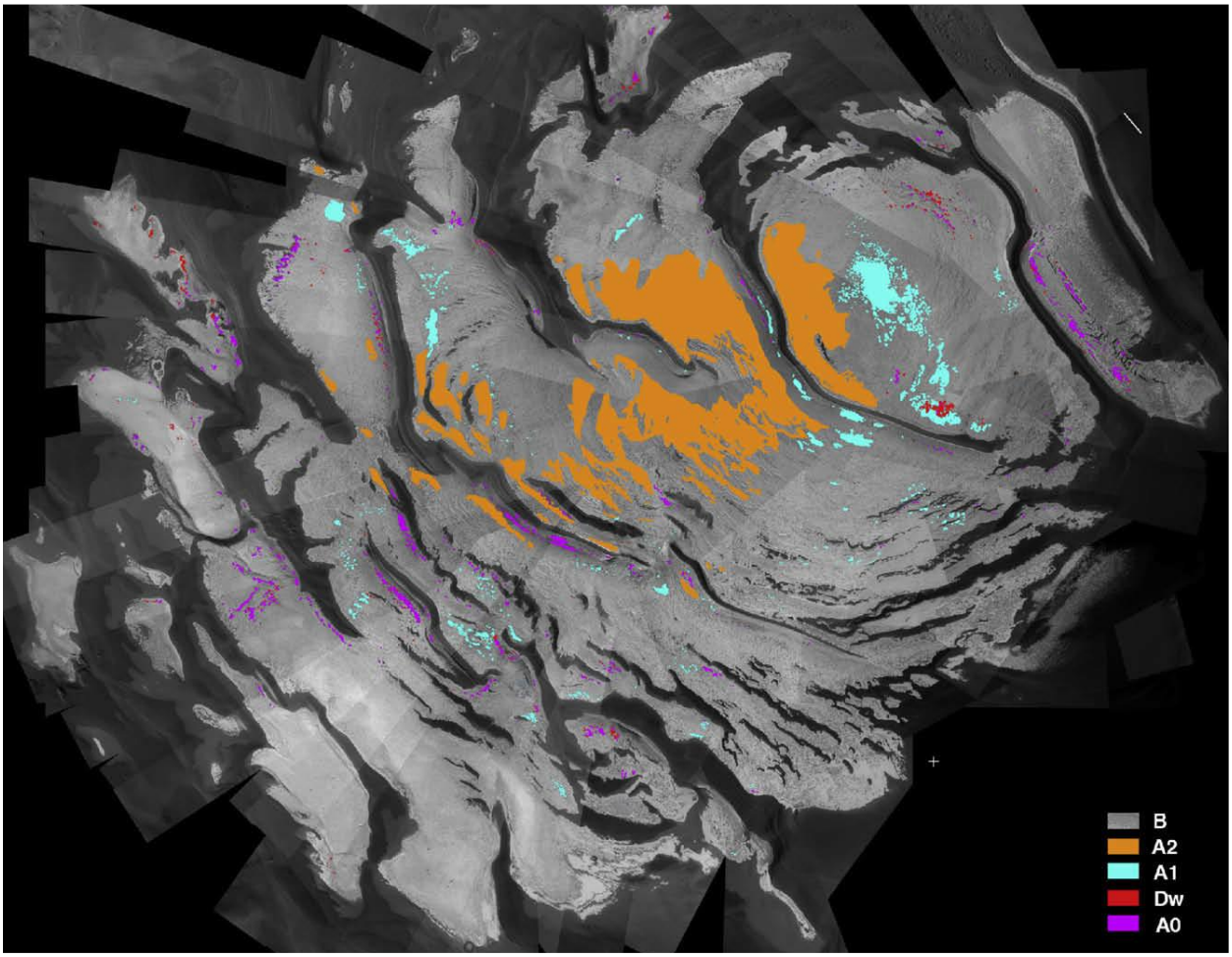

Figure 1.13: Unit map for the SPRC from Thomas et al (2009). The shaded regions represent different morphological units. Unit B is thinner, younger materials that comprise most of the SPRC. Unit A2 is 'fingerprint' terrain, long asymmetric depression. Unit A1 is the curl, heart-shaped and quasi-circular depressions of Swiss cheese terrain. Unit Dw is downwasted terrain, appearing to form from erosion. Unit A0 contains polygonal troughs and circular depressions >500m in diameter on the thickest part of the SPRC (Thomas et al, 2009).

Swiss cheese features have flat floors and steep sides and tend to be <500 m in diameter and ~8 m in depth (Thomas et al, 2000). They grow outwards at a rate of a few metres per year (Malin et al, 2001) which could lead to a total resurfacing of the SPRC by Swiss cheese growth every ~100 years (Byrne &

Ingersoll, 2003). They are formed when fractures in the SPRC either widen through sublimation or collapse into 1-2 m pits. They continue to grow outwards through sublimation of CO_2 from the walls (Buhler et al, 2017). The asymmetries in pits is likely due to insolation, with the southern wall receiving more solar radiation than the northern wall (Byrne & Ingersoll, 2003). This asymmetry can be seen in Figure 1.14.

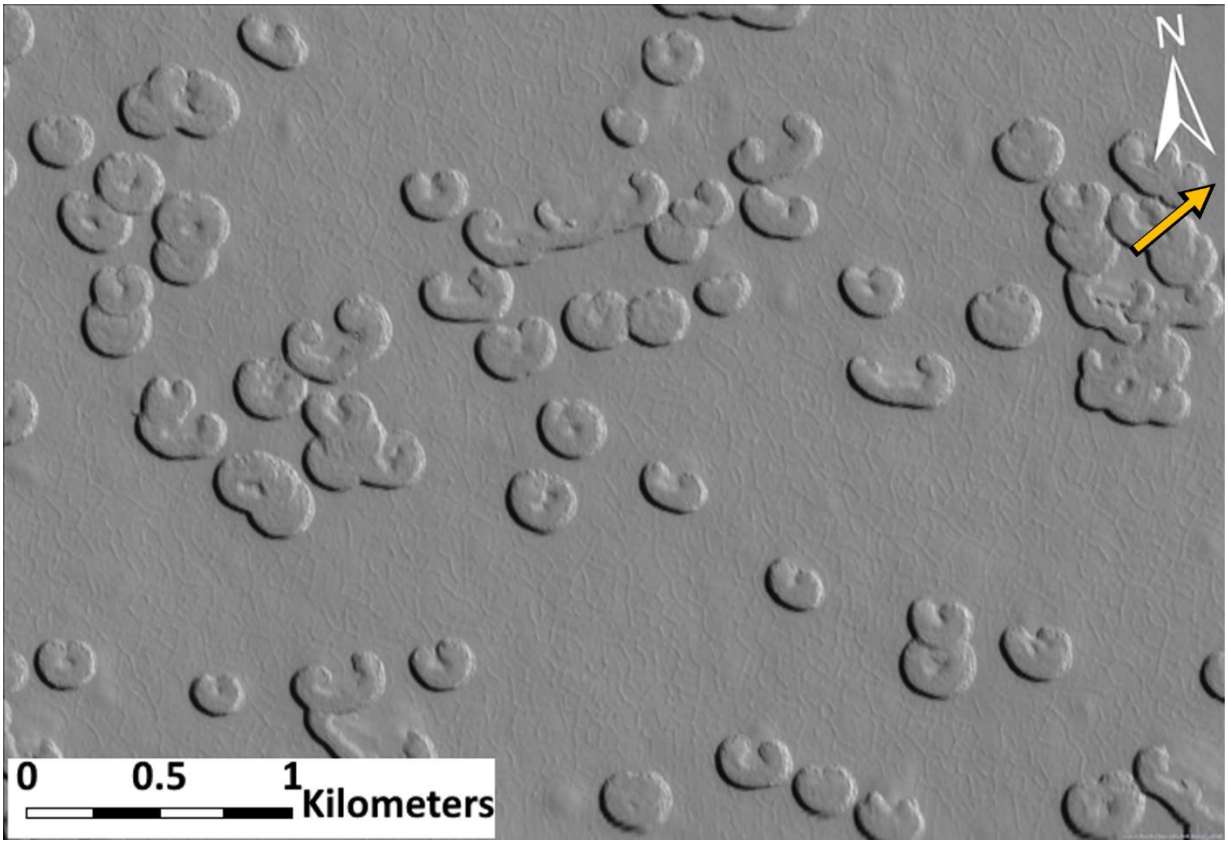

Figure 1.14: Example Swiss cheese features from the Murray lab mosaic (Dickson et al, 2018) at 86.9°S, 6.6°W. A variety of different shapes are shown from more circular features to curl shaped or branching features. Many features have more gentle northward sides compared to the steep southward sides, due to a mismatch in insolation. Direction of sunlight indicated by yellow arrow.

The southern hemisphere typically sees a gradual rise in water vapour through the southern spring through transport from the northern hemisphere. The sublimation of the seasonal polar cap in later spring leads to an increase of water vapour at high latitudes, with a maximum of water vapour abundance around L_s=290°. Water vapour abundance begins to decrease around L_s=300° over the pole, and around L_s=330°

over the entire planet (Montmessin et al, 2017). As described in Section 1.1, the peak southern summer water vapour abundance is about 20 pr µm compared to the northern summer's 60-70 pr µm (Trokhimovskiy et al, 2015), with the exception of the southern summer of 1969 (MY 8). It has been suggested that removal of most or all of the CO_2 ice of the SPRC, exposing water ice which then sublimated, could be responsible for the 1969 southern summer water vapour observation of Barker et al (1970) (Jakosky & Barker, 1984; Byrne & Ingersoll, 2003). While the Barker et al (1970) observation does have an uncertainty of about 50%, it occurs in the southern summer when we expect to see an increase in atmospheric water vapour from sublimation of polar water ice. Determining if it is possible to recreate this observation through the creation of Swiss cheese features could either support or refute the observation.

1.6 Motivation of the Thesis

The work presented in this thesis looks at two aspects of the yearly Martian water cycle in order to better understand variations within it. One aspect is the yearly Aphelion Cloud Belt, which has little interannual variability, but has been shown to be impacted by Global Dust Storms (as described in Section 1.3). The recent MY 34 GDS allows us to study Martian clouds from the surface with the Mars Science Laboratory before and after the storm. The work presented in Chapter 2 of this thesis compares the MY 34 ACB scattering phase function with that of MY 35, and is guided by the following questions:

- Did the MY 34 GDS impact the dominant crystal shape of aphelion water-ice clouds, and if so, how?
- Does the dominant ACB cloud crystal shape vary diurnally?

The second aspect is the sublimation of the south polar cap in southern summer. We are particularly interested in the magnitude of the impact Swiss cheese features may have on atmospheric water vapour,

and if these features are a plausible explanation for the unusual water vapour observation of 1969. The work presented in Chapter 3 of this thesis attempts to place an upper limit on the contribution to the Martian water cycle from Swiss cheese features. This work is guided by answering the following questions:

- How much water vapour is produced from the current configuration of Swiss cheese features?
- Is it possible to recreate the 1969 observation through partial or total removal of CO_2 on the SPRC, and if so under what conditions?

Chapter 2

Mars Year 35 Phase Function

2.1 Methods

The scattering phase function, P(Θ), describes the angular distribution of radiation scattered by aerosols – in the case of this work, water-ice clouds – as a function of scattering angle. Because of the small optical depth of the clouds, we assume there is no multiple scattering. The phase function expression derived in Cooper et al (2019) based on derivations of Kloos et al (2016) and used in this work is based on the radiative transfer equation for plane parallel atmospheres (Eq. 1.4.22 in Liou, 2002):

$$\mu \frac{dI(\tau, \mu, \phi)}{d\tau} = I(\tau, \mu, \phi) - J(\tau, \mu, \phi) \quad [2.1]$$

Where τ is the optical depth, μ is the cosine of the cloud viewing angle, ϕ is the azimuthal angle, I is the radiance from the atmosphere or cloud, and J is the source term. Since ACB clouds are assumed to be optically thin, we can use a single scattering approximation. The source term can then be simplified to (Eq. 3 in Kloos et al, 2016):

$$J(\tau, \mu, \phi) = \frac{\bar{\omega}}{4\pi} F_{\lambda,0} P(\theta) \exp\left[-\frac{\tau}{\mu_0}\right] \quad [2.2]$$

Where $\bar{\omega}$ is the single scattering albedo, $F_{\lambda,0}$ is the in-band solar flux at the cloud, P(Θ) is the phase function as a function of scattering angle (Θ), and the final term $\exp[-\frac{\tau}{\mu_0}]$ represents the transmittance through the atmosphere, with μ_0 being the cosine of the solar zenith angle. We can assume: (1) a single scattering albedo of 1 for water ice crystals in the NavCam band (eg. Liou, 2002, Fig. 5.24; Clancy et al,

2003); (2) that there is no scattering occurring above the clouds due to their height (Campbell et al, 2019); and (3) all radiance that the NavCams observe is from scattered sunlight within the cloud. From these assumptions, the downward scattered radiance from the cloud is given as follows (Eq. 6 in Kloos et al, 2016):

$$I(\Delta\tau, \mu, \phi) = \frac{\Delta\tau}{4\pi\mu} F_{\lambda,0} P(\theta) \quad [2.3]$$

Where $\Delta\tau$ is the integrated optical depth of the cloud. In order to take into account any dust between the cloud and the NavCams, we multiply by $\exp[-\frac{\tau_{COL}}{\mu}]$. τ_{COL} is taken from optical depth measurements from the MSL mast cameras (τ_{COL}) (Lemmon et al, 2015). In order to get in-band radiance, we need to multiply the radiance by the bandpass of the NavCams ($\Delta\lambda$). Equation 2.3 can then be reduced to (Eq. 7 in Kloos et al, 2016):

$$I_{\lambda,VAR}\Delta\lambda = \frac{\Delta\tau}{4\pi\mu} F_{\lambda,0} P(\theta) \exp\left[-\frac{\tau_{COL}}{\mu}\right] \quad [2.4]$$

In order to calculate the phase function, a cloud optical depth ($\Delta\tau$) needs to be assumed. We take MCS water-ice column optical depths for the area of Gale Crater, averaged over the 10° of L_s around the PFSS observations ($\Delta\tau_{MCS}$) and the last 5 Mars years. Equation 2.4 can then be rearranged to give an expression for the phase function (Eq. 5 in Cooper et al, 2019):

$$P(\Theta) = \frac{4\pi\mu I_{\lambda,VAR}\Delta\lambda}{\Delta\tau_{MCS} F_{\lambda} \exp\left(-\frac{\tau_{COL}}{\mu}\right)} \quad [2.5]$$

In order to resolve clouds in the PFSS observations, the movies undergo a process known as mean frame subtraction (MFS), which removes the time-invariant component of each frame, leaving only the time-varying component, in our case moving clouds. This is done by assembling an average frame from the three frames in each movie, which is then subtracted from each individual frame pixel by pixel. Figure 2.1 shows an example of this.

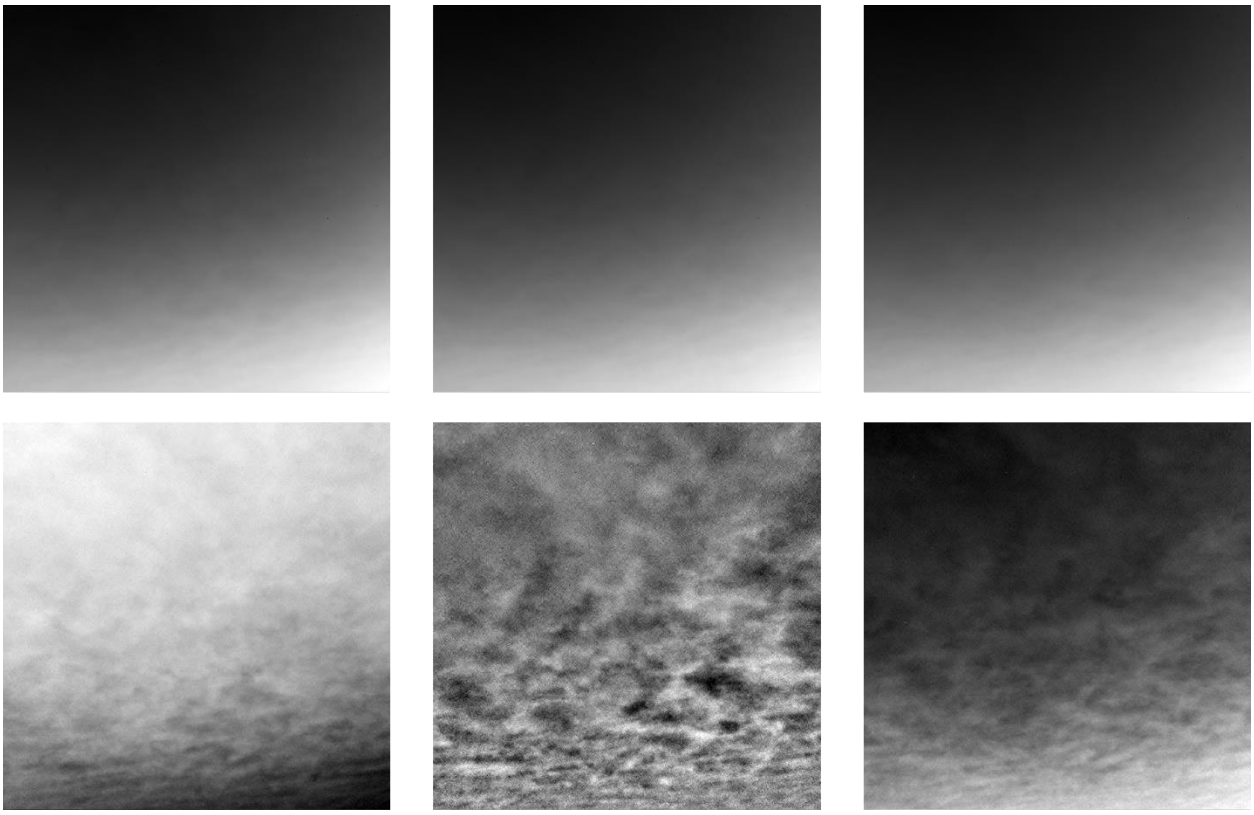

Figure 2.1: The three frames of the sol 2633 pointing 5 movie before (top) and after (bottom) mean frame subtraction. Cloud features that are not present in the raw frames are clear in the MFS frames.

Following MFS, each movie is manually examined to determine if clouds are present. If they are found to contain clouds, a radiance map of the middle frame (frame 2) is created to select a point of high and low spectral radiance, a cloudy region and an empty sky region, respectively (Figure 2.2). These regions are then averaged over a 5-pixel radius circle to determine the variation in spectral radiance, $I_{\lambda,VAR}$, used in

equation 2.5. The location of the cloud within the frame is also used to calculate the scattering angle (Θ).

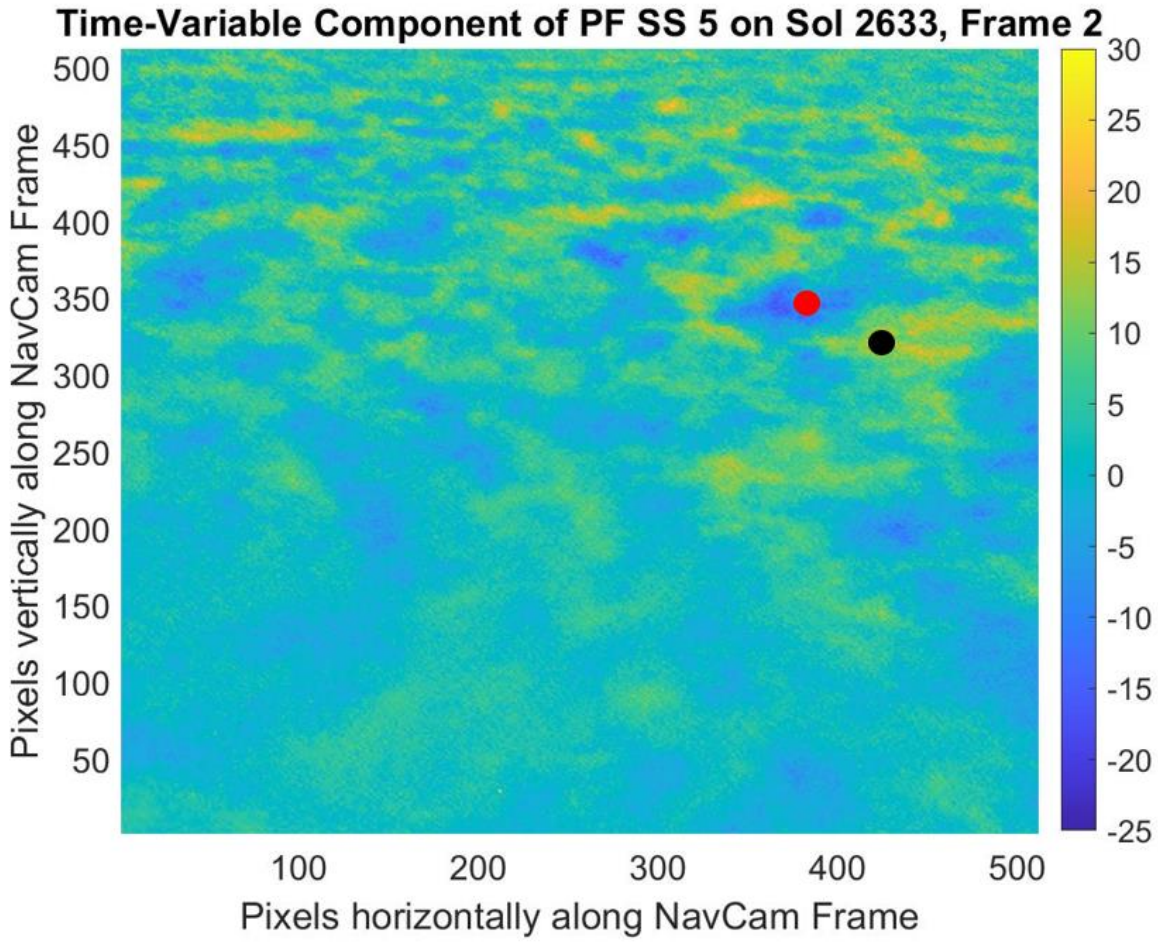

Figure 2.2: A spectral radiance map of the 2nd frame of the 5th pointing movie on Sol 2633 with a region of high spectral radiance (black dot) and low spectral radiance (red dot) indicated. The high radiance region is assumed to be a cloud while the low radiance region is assumed to be empty sky.

While the selected region of low spectral radiance is meant to be a region of empty sky, it is likely that region is instead a thinner area of the same cloud, meaning that our $I_{\lambda,VAR}$ should be taken as a lower limit, and thus the calculated phase function will also be a lower limit.

Typically, the phase function is normalised over scattering angles 0-180° such that the area under the curve is equal to 4π. However since most scattering from particles of comparable radius to Martian

aerosols occurs in the forward direction at lower scattering angles, less than 40°, it is not possible to determine what the normalisation values should be for our mean curve. However, in comparing our derived phase function with previously derived phase functions, the shape is of more interest than the absolute magnitude, and so our calculated phase function values were normalised by the average value of the Cooper et al (2019) phase function.

2.2 Analysis and Results

For the MY 35 ACB season, there were a total of 26 PFSS observations, with 13 morning and 13 afternoon observations. The morning observations occurred between 06:27 local true solar time (LTST) and 09:21 LTST, and the afternoon observations occurred between 14:30 LTST and 17:23 LTST. They spanned in L_s from 55.03° to 159.41° (sols 2471 to 2691). The temporal distribution of PFSS observations is shown in figure 2.3.

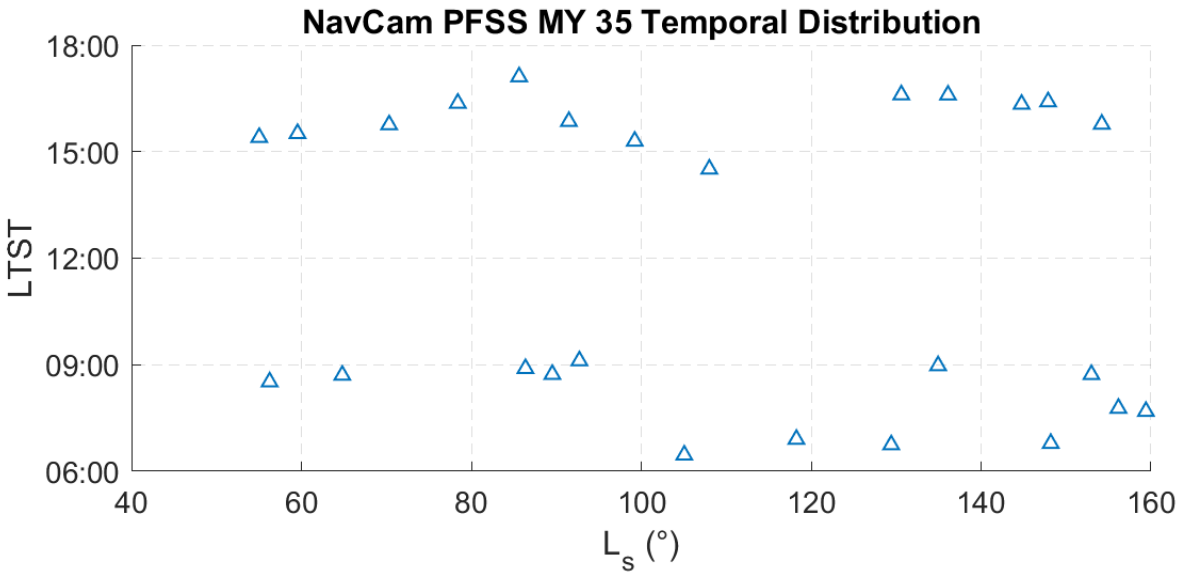

Figure 2.3: MSL NavCam PFSS observations are distributed evenly between morning and afternoon. There is a 2.5 hour keepout around local noon to avoid exposing optics to the sun.

At least one movie from each observation contained identifiable cloud features, with a total of 174 movies containing clouds features. Of these, 79 were morning observations and 95 were afternoon observations. While in some frames it was simply impossible to detect cloud features after mean frame subtraction, in others, typically those closer in time to the local noon keepout, the presence of the sun nearby created artifacts which made cloud features impossible to see even if they were present, an example of which is shown in Figure 2.4.

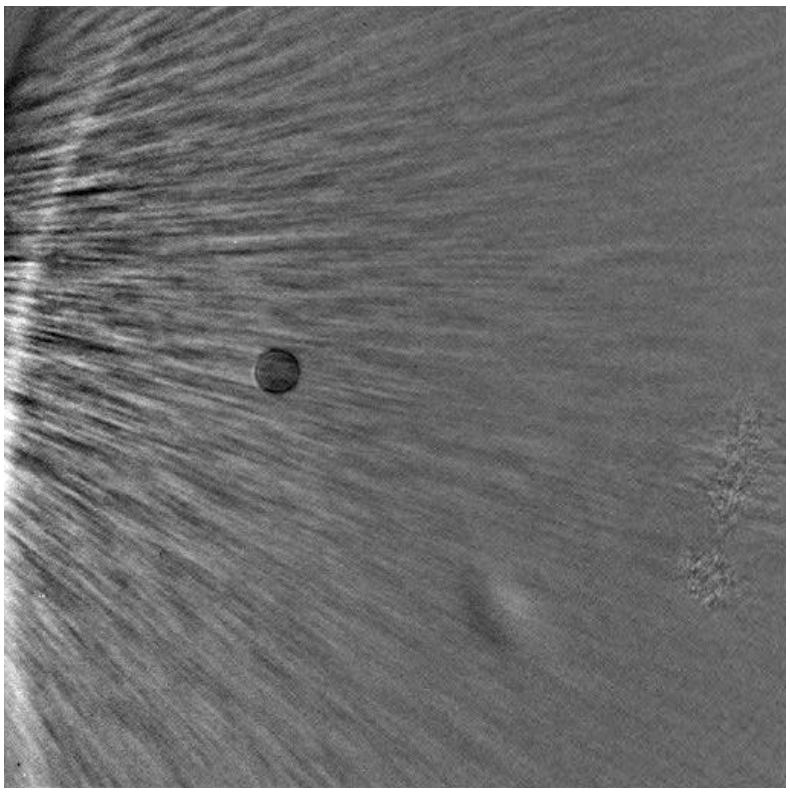

Figure 2.4: An example of an unusable frame due to proximity to the sun.
(Frame 2, Pointing 9, sol 2555, taken at 09:21:01 LTST)

The 174 data points selected from the usable movies had scattering angles between 32.9° and 154.182°, and normalised phase function values between 2.84×10^{-3} and 0.718. Of these, two data points were removed as outliers, as their phase function values were more than 3 standard deviations from the mean. These points are still plotted in Figure 2.5 (a) for completeness, but are not included in the

moving average calculation. Figure 2.5 shows the mean phase function curve, produced using a moving average with a window size of 25. The 95% confidence interval is plotted alongside the mean curve.

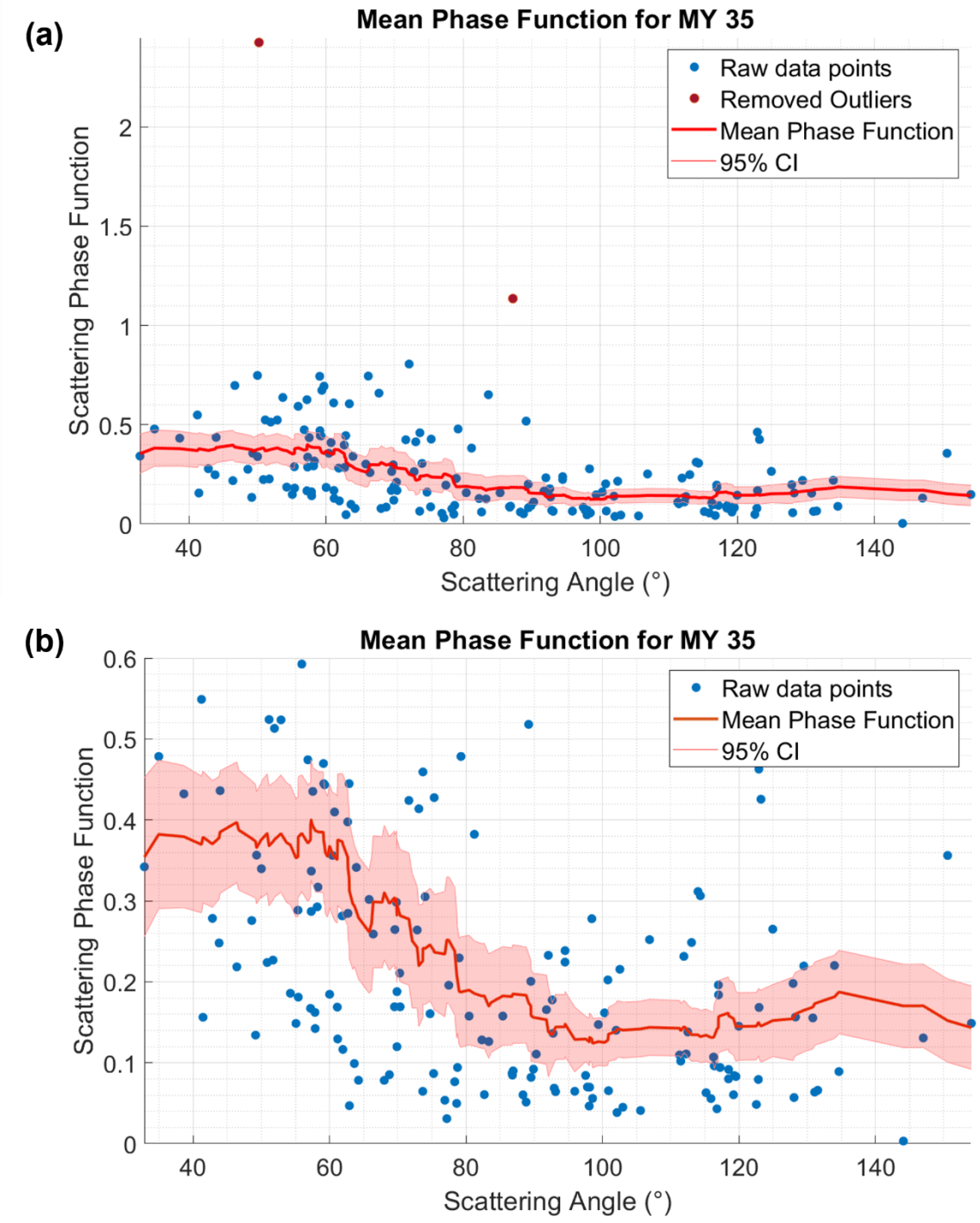

Figure 2.5: The mean phase function for Mars Year 35 displayed over the raw data points from the PFSS observation. (b) shows a zoomed in area of (a) in order to better show the features of the phase function curve. The two removed outliers are also plotted in (a).

As discussed in Section 2.1, we are not able to see scattering in the forward or backward scattering around 180°. At scattering angles greater than 100°, the curve more or less becomes flat. We also do not see the higher magnitude expected around 40°. Scattering features will be discussed in greater detail as they compare to previously derived phase functions.

The comparison of most interest in determining any effects from the MY 34 GDS is to the mean phase function derived by Cooper et al (2019) for the MY 34 ACB season in Figure 2.6.

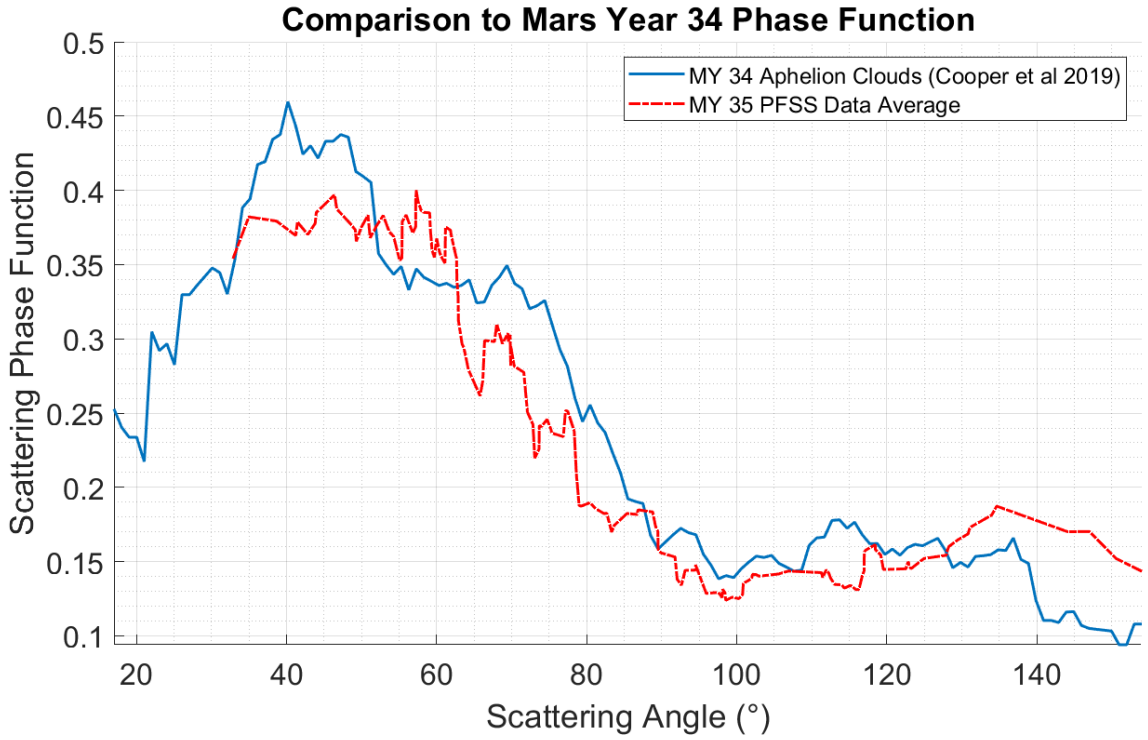

Figure 2.6: Comparison of the MY 35 average phase function with the Cooper et al (2019) MY 34 Phase Function. The mean curves have similar shapes, especially at scattering angles above ~52°.

Generally, the shapes are very similar, especially at scattering angles greater than 50°. Cooper et al reported local maxima around 22°, 46° and 70°, and minima around 50°, 100° and 140°. Our MY 35

mean curve does not reach 22°, and we do not observe the 46° maxima present in MY 34, we do see a similar maximum around 70°. As previously noted, the MY 35 curve flattens after ~100°, not showing the 140° minimum present in the MY 34 phase function. As with the MY 35 curve, that for MY 34 does not increase closer to forward scattering angles as we would expect to see.

The coefficient of determination (R^2), is given by the following expression:

$$R^2 = 1 - \frac{RSS}{TSS} \qquad [2.6]$$

where RSS is the residual sum of squares, and TSS is the total sum of squares. The R^2 value between the MY 34 and MY 35 phase functions is 0.83, indicating a fairly good match between the two over scattering angles 32.9°-154.182° (coefficients of determination for all phase functions compared in this section are given in Table 2.1). The largest difference visible in the mean curves is the difference in magnitude between ~33°-52°. The two curves are plotted with 95% confidence intervals in figure 2.7, where the error bars almost entirely overlap.

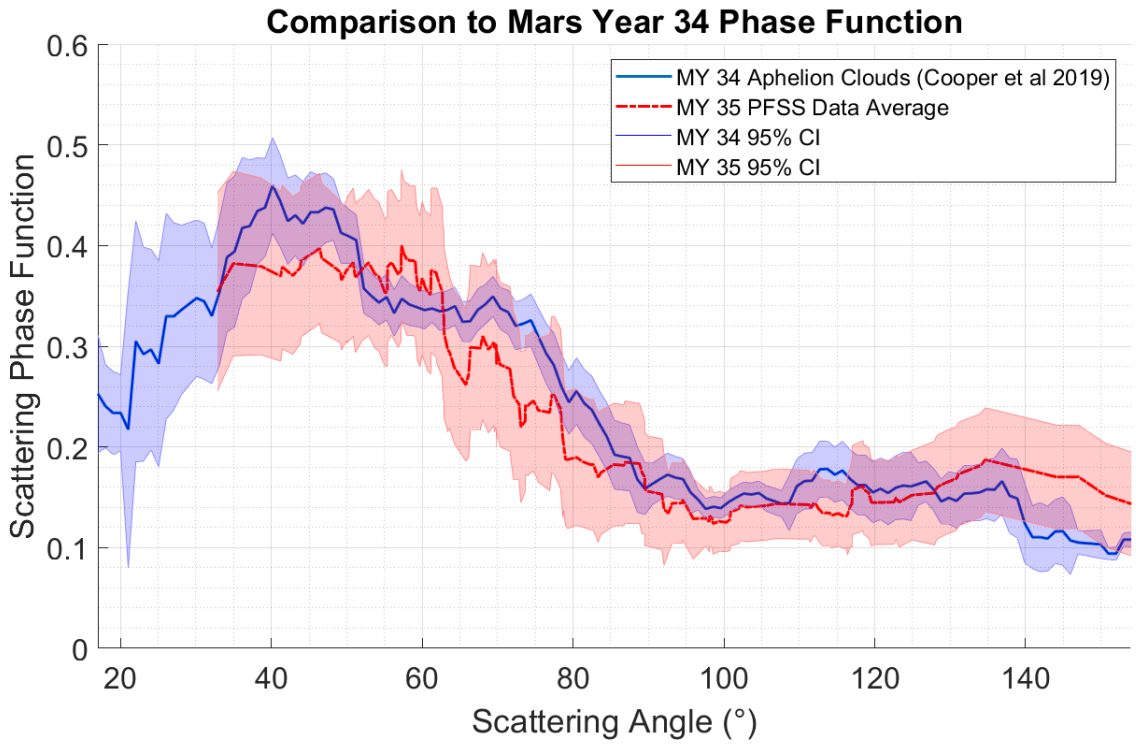

Figure 2.7: Comparison of the MY 35 average phase function with the Cooper et al (2019) MY 34 Phase Function as in Figure 2.6 with the addition of 95% confidence intervals for both curves. The great overlap between the two curves indicates a very close fit.

We also observe many of the same cloud morphologies as in the MY 34 ACB clouds. Cooper et al (2019) identified gravity waves, rippled or 'zig-zag' cloud patterns, and fractus or ragged edged clouds, all of which were also visible in the MY 35 clouds, as shown in figure 2.8.

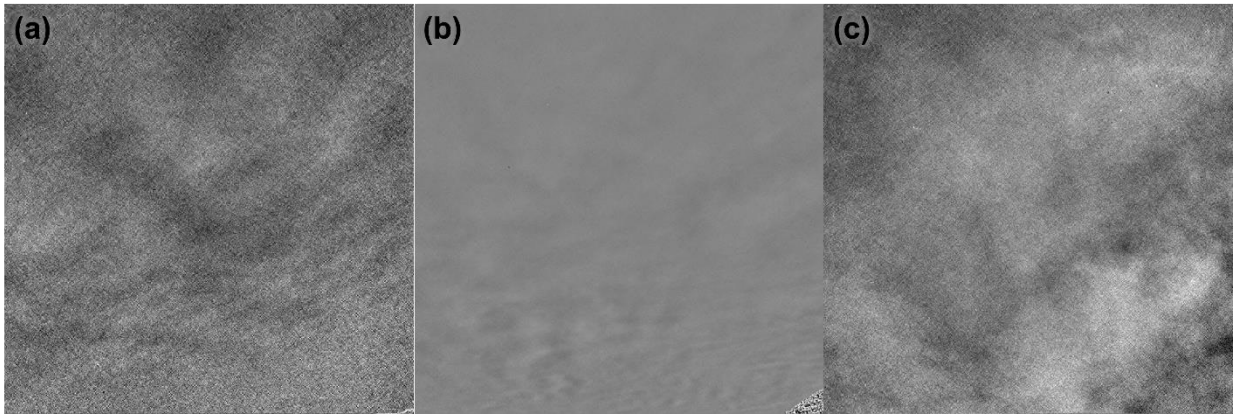

Figure 2.8: Single frames from PFSS observations showing cloud features. (a) likely gravity waves, moving from lower right of frame, taken on Sol 2541 (L_s=86°) at 08:58 LTST. (b) rippled or zig-zag clouds in the lower half of the frame, taken on Sol 2633 (L_s=129°) at 06:48 LTST. (c) fractus or ragged edged clouds taken on Sol 2582 (L_s=105°) at 06:39 LTST.

Figure 2.9 shows the comparison of the MY 35 mean phase function to four phase functions derived from observations from ITRM aboard Viking (Clancy & Lee, 1991) and TES aboard MGS (Clancy et al, 2003). While these are all phase functions of Martian clouds, only the TES observations cover ACB clouds, split into Types 1 and 2 as described in Section 1.4. It is unsurprising that the MY 35 phase function does not closely match either of the Viking curves, with R^2 values of -0.95 and -0.34.

While the fit of the MY 35 curve to the TES ACB clouds is not much better, we see in both type 1 and 2 a decrease between ~60-100° that is also present in our MY 35 phase function. However, the TES phase functions increase again after ~100° while our curve remains flat. In terms of the coefficient of

determination, the curves for type 1 and 2 aphelion clouds have R^2 values of 0.26 and 0.18, respectively, indicating as noted that the fits of these curves to our MY 35 mean phase function are not particularly good. The slightly better agreement with type 1 clouds was also noted by Cooper et al (2019), and is not unexpected, as type 1 clouds are more prominent in the southern hemisphere.

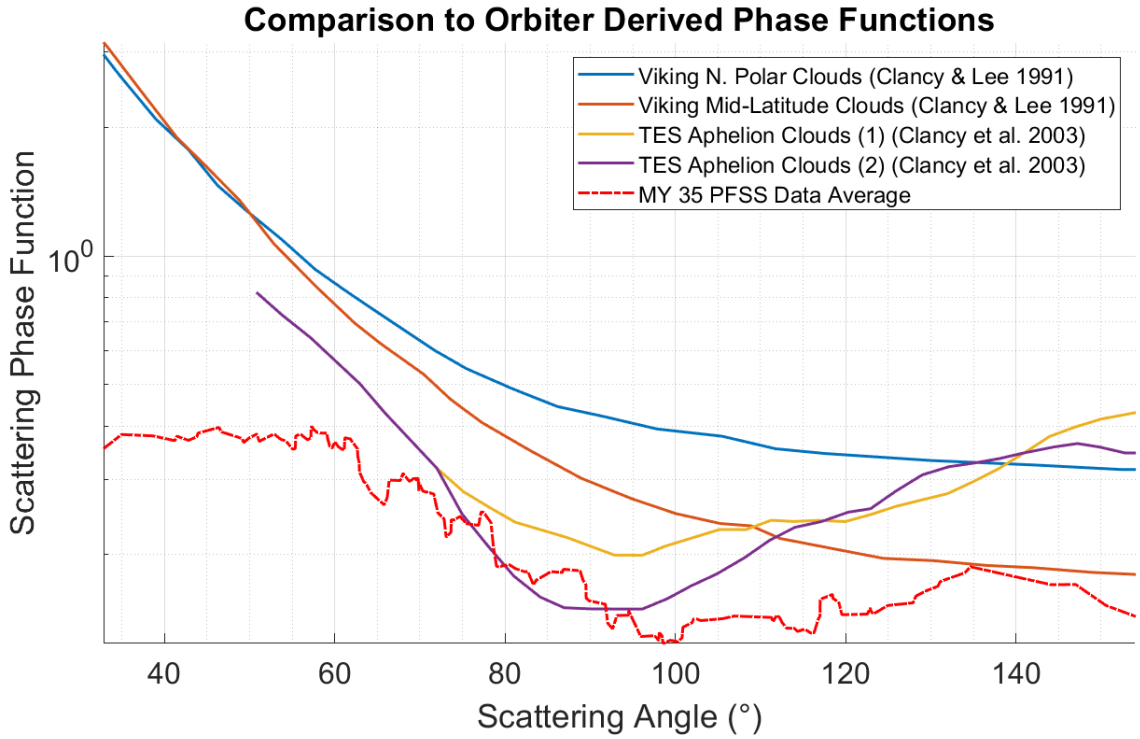

Figure 2.9: Comparison of mean MY 35 phase function with Viking and TES derived phase functions. The shape of the MY 35 mean curve, aside from being much less smooth than the orbiter curves, does not show the increase in magnitude at lower scattering angles.

The final comparison in this work is to the phase function curves of seven modeled ice crystal geometries: hollow and solid hexagonal columns, bullet rosettes, plates, aggregates, spheres (Yang & Lee, 1996) and droxtals (Yang et al, 2010). While the magnitude of energy scattered in the forward and backward directions, not shown by our curve, are more important in determining particle size, scattering at angles seen by the PFSS are more indicative of aerosol shape. Figure 2.10 shows these ice crystal geometries as compared to the MY 35 mean phase function.

From inspection, our curve does not fit any of the modeled ice crystal geometries particularly well. It is generally much flatter than the ice crystal curves, and notably missing the local maximum around 46°, already commented upon earlier in this section, that is present in the MY 34 mean phase function. Additionally, while our phase function does increase at scattering angles <100° (clearer in Figure 2.5 (b)), this increase is much less pronounced than those of the water-ice crystal phase functions, and the curve does seem to flatten out again around <60°.

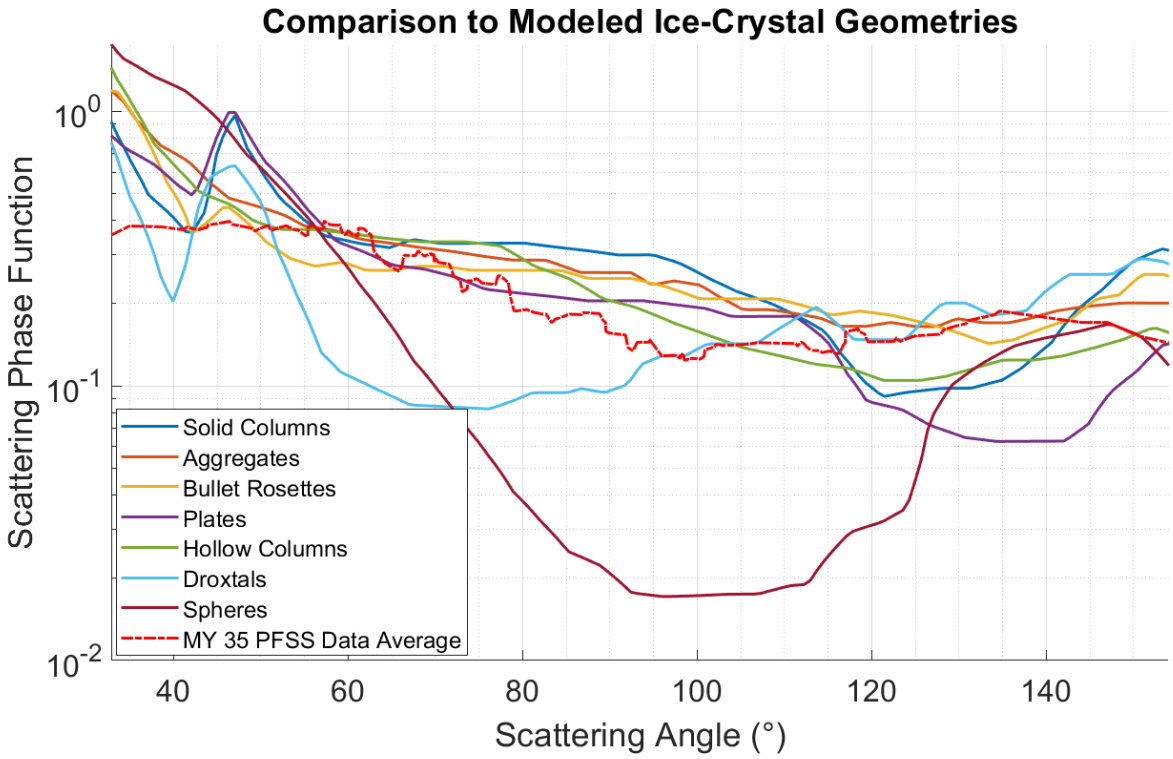

Figure 2.10: Comparison of the mean MY 35 phase function to seven water-ice crystal habits modeled by Yang & Liou (1996) and Yang et al (2010). The MY 35 mean curve does not display the local maximum at 46° present in many of the water-ice crystal phase functions.

Only solid columns have R^2 values greater than 0 (0.09), however this does not indicate a very close fit to the MY 35 phase function. The remainder of the R^2 values for the water-ice crystal phase functions (given in Table 2.1) are less than 0, indicating that the MY 35 phase function fits the data worse than a horizontal line.

Cooper et al (2019) found that some makeup of aggregates, solid and hollow columns, plates, and bullet rosettes were most likely in MY 34 ACB clouds. This agrees with the sampled makeup of terrestrial cirrus clouds (Whiteway et al, 2004). However, similarly to the MY 35 findings, none of the water-ice crystal curves fit the MY 34 phase function particularly well.

Table 2.1 *Coefficients of determination for previous modeled phase functions compared with the MY 35 mean phase function, ordered by decreasing goodness of fit.*

Compared Phase Function	Coefficient of Determination
MY 34	0.826
Type 1 Aphelion Clouds	0.258
Type 2 Aphelion Clouds	0.179
Solid Columns	0.087
Aggregates	-0.021
Bullet Rosettes	-0.149
Plates	-0.225
Hollow Columns	-0.263
Polar Clouds	-0.341
Droxtals	-0.470
Midlatitude Clouds	-0.949
Spheres	-2.686

We were interested in determining if there was any difference in the phase functions of morning and afternoon clouds. As described in Section 1.3, previous works have found differences in the optical thickness and altitude of morning and afternoon clouds (Kloos et al, 2018; Campbell et al, 2019). Of the 172 data points used for the mean phase function described above, 78 were morning observations and 94 were afternoon observations. The morning observations had scattering angles from 32.9° to 154.1°, and normalised magnitudes from 0.016 to 0.379. The afternoon observations had scattering angles from 35.0° to 144.1° and normalised magnitudes from 0.020 to 0.410. As with mean curve for all MY 35

observations, the mean curves for morning and afternoon observations were constructed using a sliding average with a window size of 25.

The mean phase functions are plotted together in figure 2.11, and separately with 95% confidence intervals in figure 2.12. The shapes of the two phase functions are very similar, both being flat until ~60°, then decreasing until ~90-100°, then flattening again, similarly to the combined My 35 phase function. Both morning and afternoon curves lie within the other's 95% confidence interval. Looking at the coefficient of determination, the R^2 value is 0.835, indicating a very good fit between the two. From this analysis there does not appear to be much difference in the phase functions in morning versus afternoon clouds.

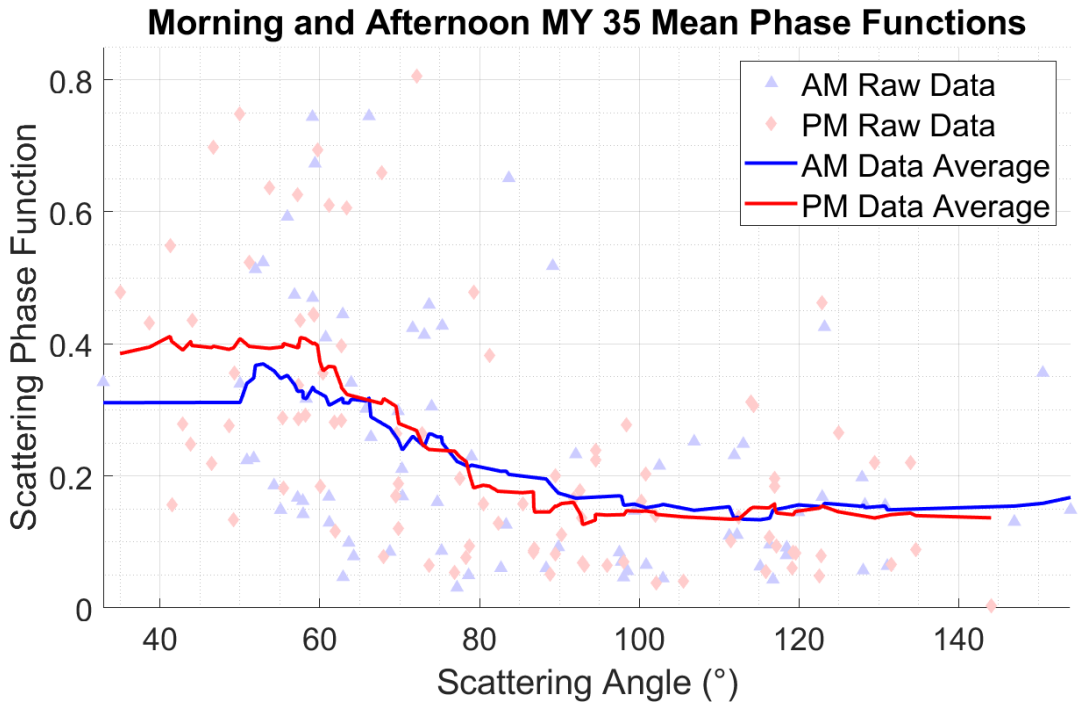

Figure 2.11: Morning and afternoon mean phase functions plotted together on top of data points in order to compare the two. The phase functions are more or less the same shapes, and fall within each others 95% confidence interval.

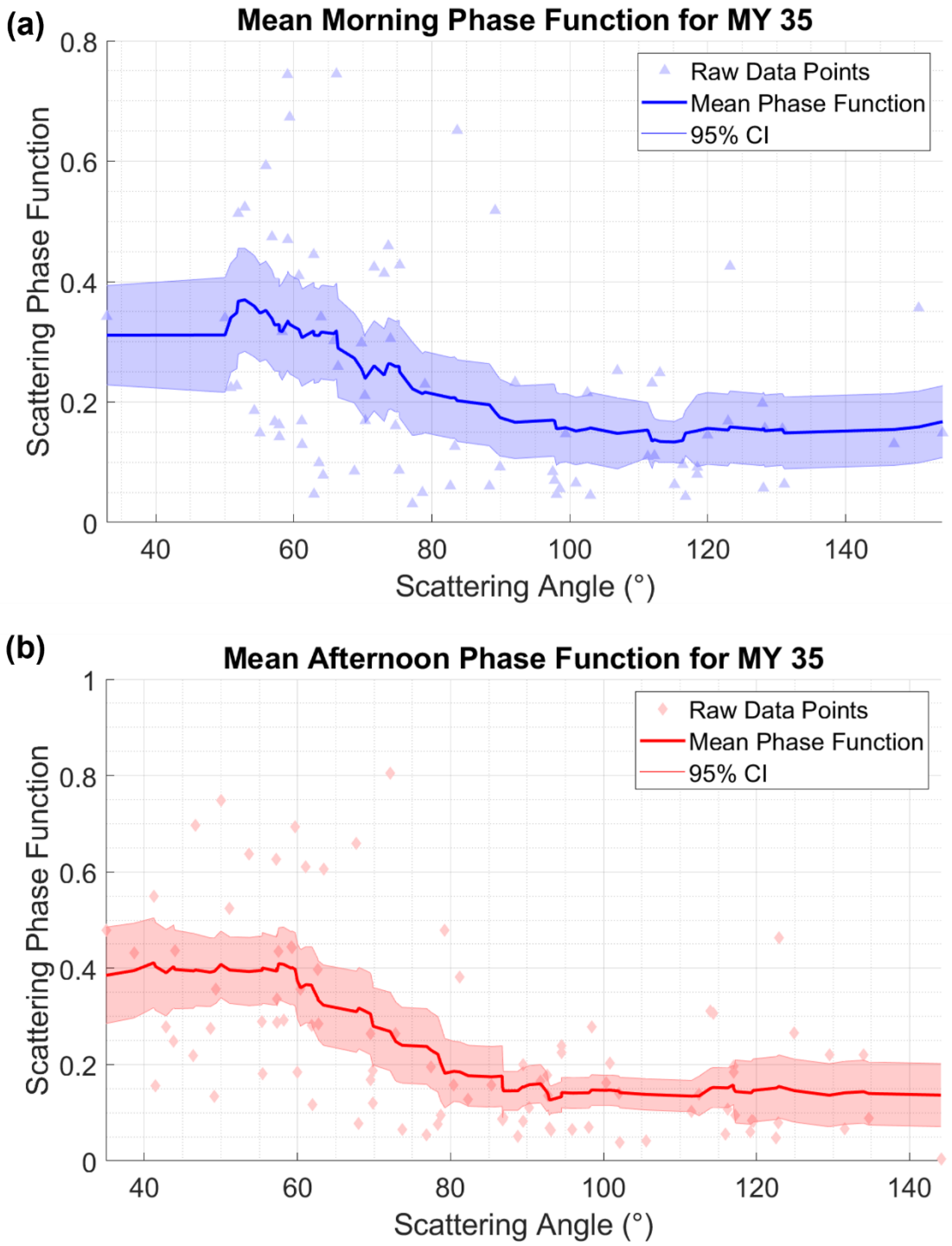

Figure 2.12: Morning (a) and afternoon (b) mean phase functions for the MY 35 ACB season with 95% confidence interval, plotted over data points.

2.3 Discussion

The main discrepancy in our mean phase function is the lack of increase towards the forward scattering direction. We see this increase in the modeled phase functions of the seven water ice crystals (Figure 1.11), as well as in the Viking and TES derived phase functions (Figure 2.9), as well as Martian dust phase functions (eg. Tomasko et al, 1999), but it is missing from both the MY 35 and MY 34 phase functions.

While the PFSS observation cannot see scattering angles close to 0°, we would still expect to see an increase in the magnitude of the phase function at scattering angles below 40°, which are included in both our phase function and the Cooper et al (2019) phase function. In fact, the MY 34 phase function has a minimum scattering angle of 18°, yet does not show the marked increase in magnitude we would expect.

It is likely that the lack of a forward scattering increase is not an actual part of the scattering properties of the ACB clouds, especially given that other Martian water-ice clouds phase functions see this increase. Instead, it is more likely that it is a result of the method used to derive the phase function. It is currently unclear whether this is due to the PFSS observation itself or to our method of calculating the phase function. It may be the case that this discrepancy is due to the difficulty capturing frames too close to the sun, as seen in Figure 2.4.

Our phase function also does not seem to match any of the modeled ice-crystal phase functions particularly well, as can be seen in Figure 2.10 and in the calculated R^2 values. This could be due to the clouds being composed of a mix of different ice crystal morphologies, as in terrestrial cirrus clouds. The phase functions of terrestrial thin cirrus clouds do not match any one ice crystal phase function either, and are relatively flat between 90-180° (Wang et al, 2014).

However, it could also be the case that Martian water-ice clouds contain water-ice crystal morphologies that differ from those of terrestrial water-ice clouds. The lack of a good agreement between our phase

function and any of the modeled ice crystal morphologies could suggest that the dominant ice crystal habit of the clouds we observe is not one of these. Given the different conditions of the Martian atmosphere, it is possible that different formation mechanisms lead to different ice crystal morphologies.

Another aspect of the phase function we do not explore in this work is any seasonal variation. Kloos et al (2018) saw differences in the optical depth of clouds in the early and late ACB season, as described in Section 1.3. Our mean phase function, and our mean morning and afternoon phase functions are averaged over the entire ACB season, over 100° of L_s. In doing this we are missing any potential changes over the course of the season. This could mean missing potential scattering features that are only present at certain times of the season, and creating a flatter curve over the whole ACB season. It is also possible that as we saw with the morning and afternoon phase functions, there is little seasonal variation. Kloos et al (2018) and Campbell et al (2020) both saw diurnal variations in optical depth and altitude, while we saw no variations in phase function, indicating that the ice crystal habit remains the same throughout the sol. The same could be true for seasonal variation.

The nature of the PFSS observation limits our phase function determination. We are not able to observe close to the sun, and thus lose scattering angles near 0° and 180°, where we get information about particle size. Observing clouds close to the sun is also problematic, as the sun is 10^6 times as bright as typical Martian clouds, but being able to observe these clouds would allow us to have a more complete idea of the scattering properties of the ACB clouds. Due to the restrictions on viewing clouds near the sun, we are also unable to take PFSS observations around noon, which prevents us from including midday clouds in our phase function calculation.

Additionally, using the MCS retrievals for the clouds optical depth may not be a perfect estimation. The MCS atmospheric retrieval does not reach the lower few kilometers of the atmosphere, and many of the

water-ice opacity retrievals only reach down to about 30 km above the surface. As ACB clouds are more likely to form between 15-30 km, it is possible MCS is seeing a sperate cloud deck than that we observe from the surface. If this is the case, the optical depth values we are using in the phase function calculation may be lower than the actual optical depth, which would give us a higher phase function value, as optical depth is inversely proportional to phase function. In addition, we take MCS optical depth values averaged over 10° of L_s, which means we are not taking the actual optical depth of the clouds observed in each PFSS. The sun-synchronous orbit of MRO means that MCS observes Gale crater at the same time every day, and does not capture any variability in clouds at different times of day. We also know that the value of $I_{\lambda,VAR}$ is a lower bound value, as described in section 2.1, which in turn gives us a lower phase function value.

The lack of a difference in morning and afternoon phase functions seems to suggest that the dominant ice crystal geometries are the same for morning and afternoon clouds. However this could also be a function of the fact that the optical depths used do not distinguish between morning and afternoon values. Kloos et al (2018) found differences in the optical depths of morning and afternoon clouds, and as the phase function is dependant on the cloud optical depth, it could be that our using an average value of optical depth artificially creates the similarities between the morning and afternoon mean phase functions.

Chapter 3

Atmospheric Water Vapour Contributions from Swiss Cheese Terrain

3.1 Methods

In order to map individual Swiss cheese features on the SPRC, we used images from the Mars Reconnaissance Orbiter (MRO) Context Camera (CTX). The CTX has a resolution of 5-6.5 m/pixel and is intended to provide context images for other MRO instruments, as well as observe the terrain of Mars (Malin et al, 2007). We used the Murray Lab mosaic in ArcMap, a blended mosaic of CTX images with a resolution of 5 m/pixel (Dickson et al, 2018), in ESRI ArcMap 10.7.1.

In order to identify areas of Swiss cheese terrain, we used the Thomas et al (2009) unit map (Figure 1(A) in Thomas et al, 2009; duplicated in Figure 1.12) overlaid on the CTX mosaic (Figure 3.1). Of the sites identified, any smaller than 0.5 km^2 were excluded because of the uncertainty in determining the exact margins for sites this small from the Thomas et al (2009) map. Because no shape file was available for the Thomas et al (2009) unit map, the figure had to be overlaid on the CTX mosaic (as shown in Figure 3.1), which had a much lower resolution (~20 m/pixel) and unclear margins for shaded units. Additionally, the footprint for surface temperature retrievals (described later in this section) is 36 km^2, and sites this small will not contribute significantly to the overall temperature of the retrieval, as the site itself will be less than 1.4% of the total footprint.

Polygons are drawn in ArcMap to map the Swiss cheese features within the remaining sites. For sites less than 10 km^2, the entire site was mapped, but in order to save time for those larger than 10 km^2, only about 25% of site was mapped in order to derive a representative sample of Swiss cheese pit area versus high standing CO_2 ice.

Some of the Swiss Cheese features contain interior raised areas which we called ‘mesas’. These are high standing areas assumed to be remenants of the SPRC (Buhler et al, 2017), and were mapped and excluded from the final total area of Swiss cheese features. This allowed us to determine a fraction of terrain carved out of the SPRC by negative topography features within each Swiss cheese site.

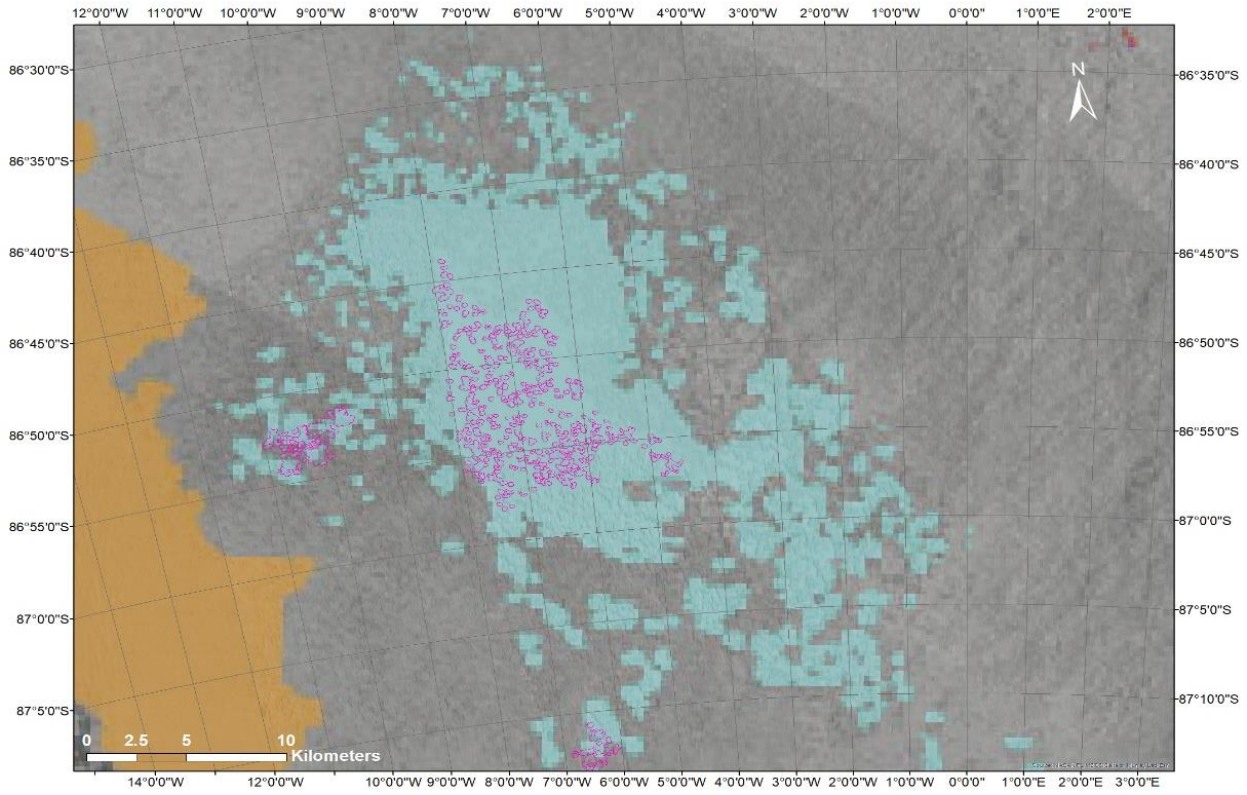

Figure 3.1: The Murray Lab CTX mosaic (not shown) overlaid with the Thomas et al (2009) unit map. The cyan area represents unit A1, and the magenta polygons are Swiss cheese features mapped in ArcMap. The grey background is Unit B and the orange is Unit A2.

We then used surface temperature retrievals from the Mars Climate Sounder (MCS) to determine any secondary temperatures present within a site. MCS is an infrared radiometer aboard the Mars Reconnaissance Orbiter (MRO) which takes atmospheric and surface measurements of various properties such as vertical temperature and pressure profiles, surface radiance and aerosol properties (McCleese et al, 2007). It uses in-track limb staring to derive atmospheric profiles, as a result of which the footprint for surface retrievals is not at the spacecraft (shown in Figure 3.2).

MCS has a calibration requirement of better than ±0.5% at 300 K, which it maintains by frequent in-flight calibrations (McCleese et al, 2007). Channel B1 (centered on 31.7 µm), which is used for surface temperature retrievals, has an absolute error of less than ±1 K at 150 K (Hayne et al, 2012), and all retrieved surface temperatures used in this work had reported uncertainties less than ±0.1 K. Pressure retrievals are based on the ratio of radiances in the A2 and A3 channels (centered on 15.9 µm and 15.4 µm respectively) and have a precision of 1–2% (Kleinböhl et al, 2009).

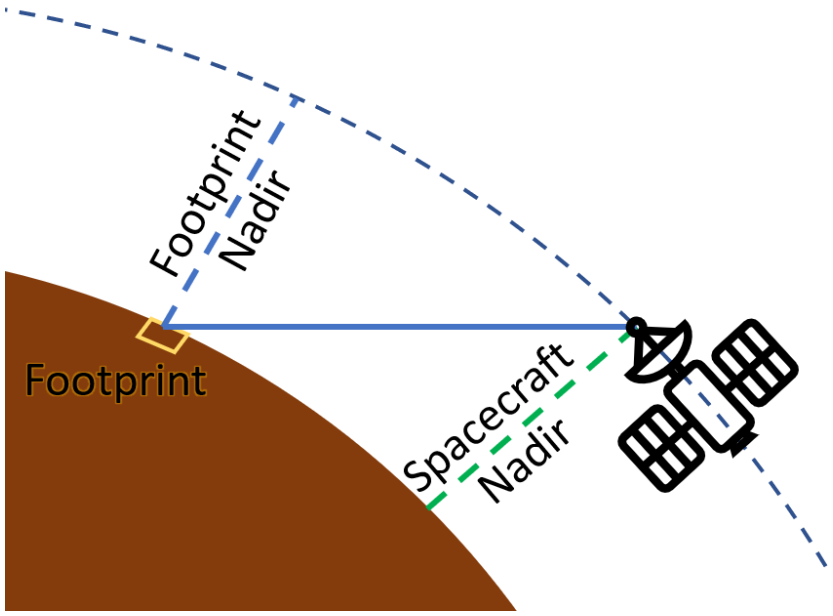

Figure 3.2: MCS in limb staring mode, retrieves surface brightness temperature from surface infrared radiance and broadband solar reflectance at a non-zero emission angle.

As MCS has a footprint of 6x6 km (eg. Hayne et al, 2012), we only looked at sites that were greater than 20 km^2 to ensure that the Swiss cheese terrain filled most of the footprint, as well as being at least 6 km away from any troughs to eliminate any effects from their starkly different albedo from the SPRC surfaces. The MCS temperature retrieval is a brightness temperature of the whole scene, and in order to calculate the CO_2 frost temperature within the scene, the MCS surface pressure retrieval (P_{surf}) was also used (eq. 3.1).

$$T_{CO_2} = \frac{-\beta}{\ln(P_{surf}) - \alpha} \quad [3.1]$$

Where α=23.3494 and β=3182.48, and P_{surf} is in mbar (James et al, 1992). A scene emissivity could then be determined using the expression:

$$\varepsilon_{scene} = \frac{T_b^4}{T_{CO_2}^4} \quad [3.2]$$

Where T_b is the retrieved MCS brightness temperature. Any scene emissivity less than 1 was assumed to contain only CO_2 ice, while a scene emissivity greater than 1 indicated the presence of some other material in the scene, as a single component CO_2 surface cannot physically have an emissivity greater than 1. This secondary material is assumed to be water ice based on the following conclusions of previous work. Byrne & Ingersoll demonstrated in their 2003 paper that a model of H_2O ice below ~10 m of CO_2 best recreates observations of Swiss cheese feature creation and expansion. Additionally, CRISM data has shown water-ice in the walls and floors of some Swiss cheese features (Cartwright et al, 2021). Finally, our derived MCS water ice temperatures (presented in section 3.2) are for the most part in the same range as retrieved THEMIS water-ice temperatures for Swiss cheese terrain, presented in Byrne & Ingersoll (2003), demonstrating cross data set consistency in our inferred temperatures.

A linear subpixel mixing model was then used to determine what temperature of the water-ice would be required to reproduce the retrieved MCS surface temperatures. The total brightness temperature of the scene is calculated first by determining the total radiance from CO_2 and H_2O components within the MCS footprint such that:

$$R_\lambda = f\varepsilon_{H_2O}B_\lambda(T_{H_2O}) + (1-f)\varepsilon_{CO_2}B_\lambda(T_{CO_2}) \quad [3.3]$$

Where R_λ is the retrieved scene radiance, f is the fraction of the scene taken up by water-ice, ε_{H2O} is the emissivity of water ice (0.987 from Warren et al (1990)), $B_\lambda(T_{H2O})$ is the black body radiance from water-ice, ε_{CO2} is the CO_2 emissivity (0.9 based on calculated scene emissivities), and $B_\lambda(T_{CO2})$ is the black-body radiance from CO_2 ice. An upper-bound on the fraction of water-ice present was taken as the mapped fraction of Swiss cheese features within a given scene.

From our derived water-ice temperature (T_{H2O}), we can then determine a sublimation rate of the exposed water-ice. The saturation vapour pressure (P_s) at the ice-atmosphere boundary for a given temperature of water ice is given by the Clausius-Clapeyron equation (based on equation 5 in Schorghofer, 2008):

$$P_s = P_t \exp\left[-\frac{\Delta H}{R}\left(\frac{1}{T_{H_2O}} - \frac{1}{T_t}\right)\right] \quad [3.4]$$

Where P_t is the triple point pressure of water (611 Pa), ΔH is the change in enthalpy (51.058 kJ kg^{-1}), R is the universal gas constant (8.3145x10^{-3} kJ mol^{-1} K^{-1}), and T_t is the triple point temperature of water (273.16 K). We can then use the saturation vapour pressure to compute a mass loss rate ($\bar{J}$) into vacuum in kg m^{-2} s^{-1}:

$$\bar{J} = P_s\sqrt{\frac{2m}{\pi k_b T_{H_2O}}} \quad [3.5]$$

Where m is the mass of one water molecule (2.988×10^{-26} kg) and k_b is the Boltzmann constant (1.3806×10^{-23} m^2 kg s^{-1} K^{-1}).

From this calculated mass flux and using our mapped Swiss cheese feature area as an observational constraint on f in equation 3.3, we can determine an order of magnitude estimate of mass loss from Swiss cheese terrain in its currently observed configuration, assuming the Martain atmosphere is sufficiently dry that sublimated water vapour is instantly transported away, as in a vacuum. This framework can then be extended to a situation in which the entire SPRC is carved out be Swiss cheese features, exposing water ice. The 1969 observation saw 45-50 pr μm of water vapour above the south pole (Barker et al, 1970), approximately twice the typical southern hemisphere peak for water vapour abundance.

We can determine the water vapour column abundance (PW, precipitable water) from the mass of water vapour released ($\mathrm{m}_{\mathrm{H_2O}}$) using the expression:

$$PW = \frac{1}{A}\left(\frac{m_{H_2O}}{\rho_{H_2O}}\right) \quad [3.6]$$

where A is the area of interest, and $\rho_{\mathrm{H_2O}}$ is the density of liquid water. We can also determine the partial pressure of the sublimated water vapour using:

$$P_{H_2O} = \frac{m_{H_2O}}{A} g \quad [3.7]$$

Where g is the acceleration due to gravity (3.71 m s^{-2} on Mars). This quantity can be compared with the saturation vapour pressure (SVP) of water vapour in the atmosphere:

$$SVP = 10^{\left[-\frac{2663.5}{T}+12.537\right]} \quad [3.8]$$

adapted from equation 1 in Marti & Mauersberg (1993) where T is the temperature of the atmosphere. If the partial pressure of the sublimated water vapour is less than the SVP, it is more reasonable to assume that the atmosphere is dry and that downward flux of water vapour is negligible. If the partial pressure is greater than the SVP, then we will likely have condensation of water molecules back onto the surface of the SPRC. This is an important condition in testing our assumption that the Martian atmosphere is essentially dry with respect to water vapour in the sublimation rate calculation.

3.2 Analysis and Results

There are a total of 83 sites of Swiss cheese terrain identified from the Thomas et al (2009) unit map that were greater than 0.5 km^2, for a total site area of 1627.8 km^2 with the smallest being 0.7 km^2 and the largest being 472.2 km^2. Of these sites, four contained features that did not resemble typical Swiss cheese terrain, and were excluded from mapping. A typical example is presented in Figure 3.3.

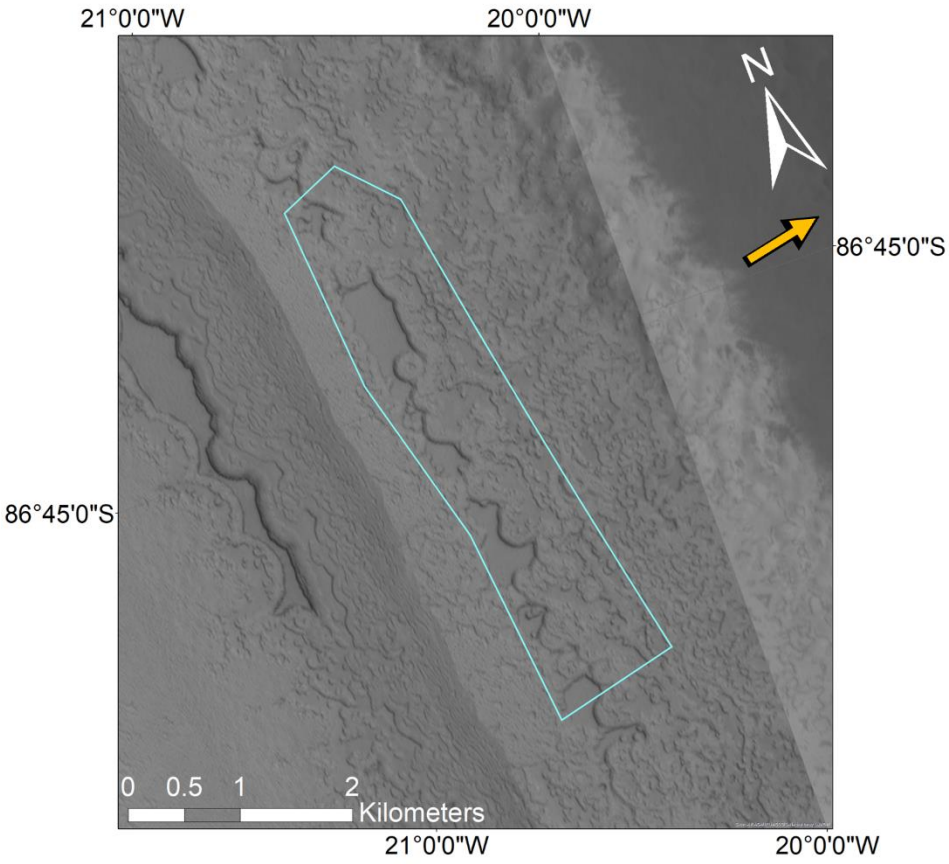

Figure 3.3: An example site that was rejected for mapping. In addition to being too near to a trough(the dark feature in upper right corner) for temperature retrieval, it was difficult to identify where recognisable Swiss cheese features graded into the non-Swiss cheese nearby terrain. Direction of sunlight indicated by yellow arrow.

As all four of these sites also fell below the minimum size for temperature retrieval, and most were near troughs, their exclusion did not impact the sublimation calculations. The total area of the SPRC was mapped to be 86572.42 km^2 (Tanaka & Scott, 1999). The total mapped area of Swiss cheese features was 184.17 km^2, or 0.213% of the total area of the SPRC. The average ratio of Swiss cheese features to surrounding terrain within unit A1 sites was 42.8%, and varied from 11.5% to 85.0%.

Twenty sites had areas greater than 20 km^2, and of these sites 14 were sufficiently far from a trough and had more than one surface temperature retrieval from MCS. Troughs have a significantly different albedo from the surrounding SPRC which means we cannot assume that they have the same thermal

properties as pure CO_2 ice. Thus, we avoided retrievals that may have included troughs in the footprint. These 14 sites were further narrowed down to five with a scene emissivity of greater than 1, which was our benchmark for the presence of water ice, as shown in Figure 3.4.

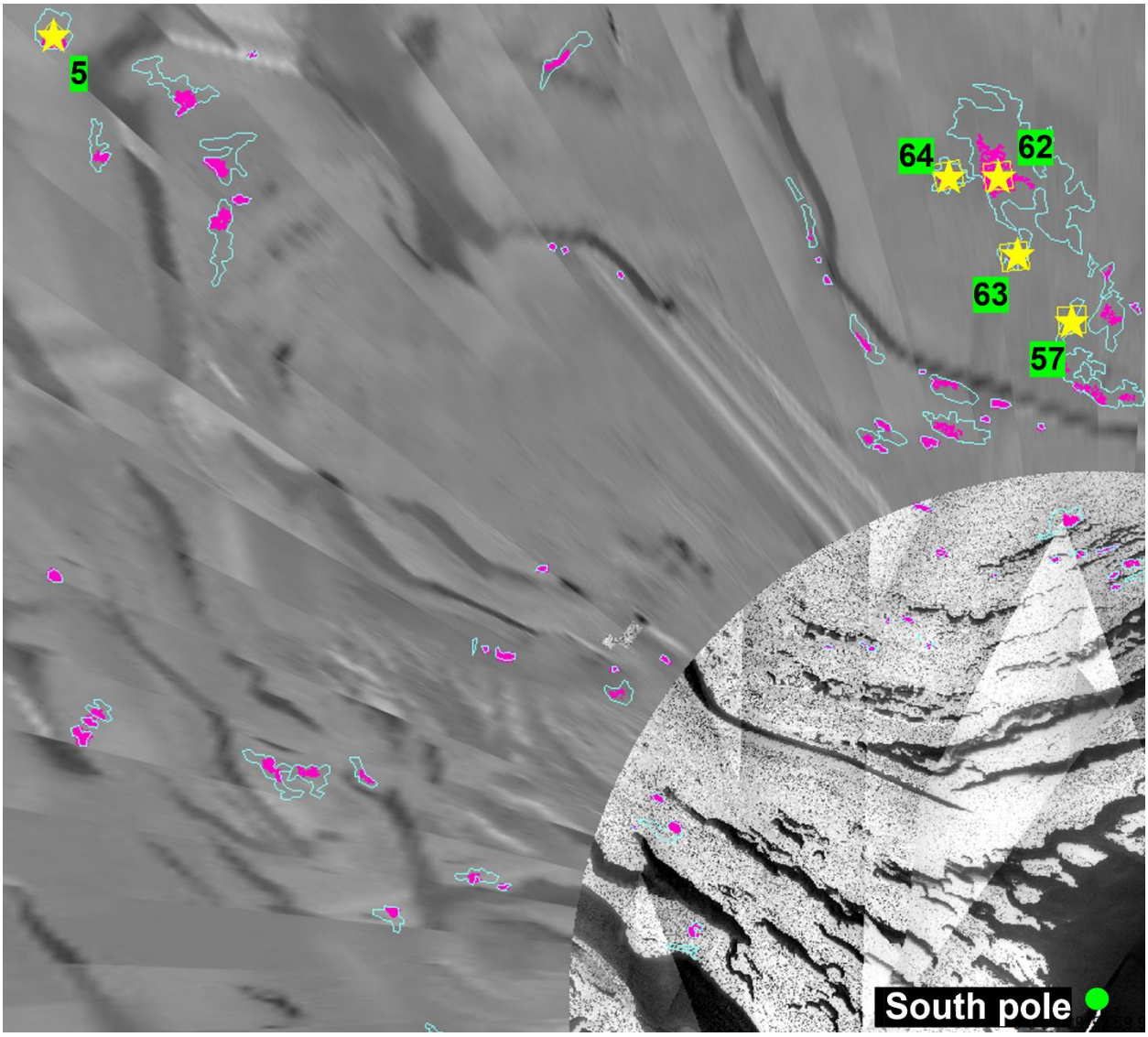

Figure 3.4: CTX Mosaic of the SPRC with mapped sites of Swiss cheese terrain. Cyan indicates site of Swiss cheese terrain, with magenta being individual mapped Swiss cheese features. Yellow stars indicate sites that suggest the presence of water ice, with their site numbers. The south pole is indicated by the green dot.

Subpixel mixing plots were created for each of the sites using the mean summer CO_2-ice temperature as a reference temperature (T_{CO2} in equation 3.3). Sites 57, 63 and 64 have reference temperatures of

144.3 K, while site 62 has a reference temperature of 143.3 K and site 5 has a reference temperature of 146 K. The subpixel mixing plots are shown in Figures 3.5-3.9. The majority of the derived water-ice temperatures fall between 150 K and 180 K. As described in Section 3.1, these temperatures (150-180 K) agree with Thermal Emission Imaging System (THEMIS) observations presented by Byrne and Ingersoll (2003) of Swiss cheese depression floors (Figure 3 in Byrne and Ingersoll, 2003).

There are five inferred water ice temperatures above 190 K, much higher than other inferred water ice temperatures, which also correspond to site emissivities of ~1.5 and above. It is unclear what is causing these unusually high retrievals. The retrieved MCS temperature and pressure errors for these anomalous observations all fall within the range of variations seen in the nominal observations. There does not appear to be a temporal connection to the anomalous observations, as they are distributed throughout the southern summer and the six Mars year over which the observations are taken (Table 3.1). While one anomalous observation falls in MY 34, after the global dust storm, so too do several more observations resulting in more typical temperatures. We took retrieved MCS dust optical depths for the Swiss cheese sites, and were not able to find a connection between optical depth and brightness temperature. Additionally, looking at the cut-off elevations of the retrievals, none are sufficiently high to indicate unreliable retrievals, and thus it is unlikely that these higher temperatures are the result of problems with the instrument (Piqueux, personal communication, 2021).

We have chosen to include these points for completeness in our calculations as outliers. Because of the large thermal gradient between these high water-ice temperatures and the surrounding CO_2 ice (between 143-146 K), it is unlikely that these temperatures are sustainable over the southern summer, however modelling beyond the scope of this chapter would be required to understand what thermal conditions these water-ice temperatures could be sustained under. Further discussion of resolving these anomalous observations can be found in Chapter 5.

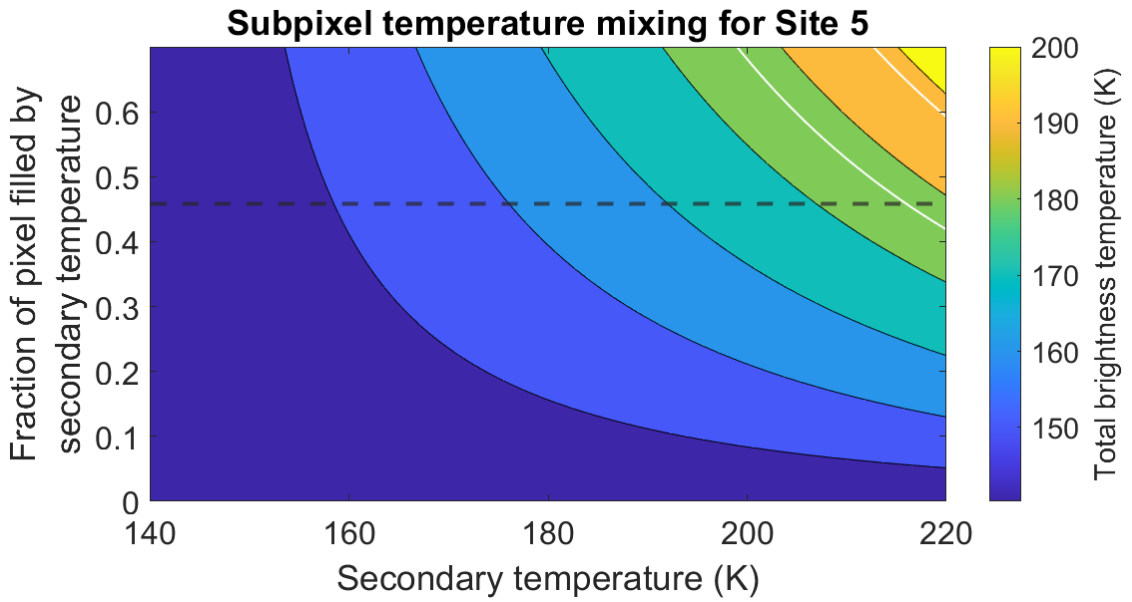

Figure 3.5: Subpixel temperature mixing plots for Swiss cheese terrain site 5, with a CO_2 ice temperature of 146 K. White contour lines represent the MCS retrieved brightness temperatures, and the dashed line represents the mapped fraction of Swiss cheese features. Where the contours cross the dashed line gives the secondary (water-ice) temperature for that fraction of exposed water ice. The only two retrievals indicative of water-ice in site five were outliers with water-ice temperatures greater than 200 K.

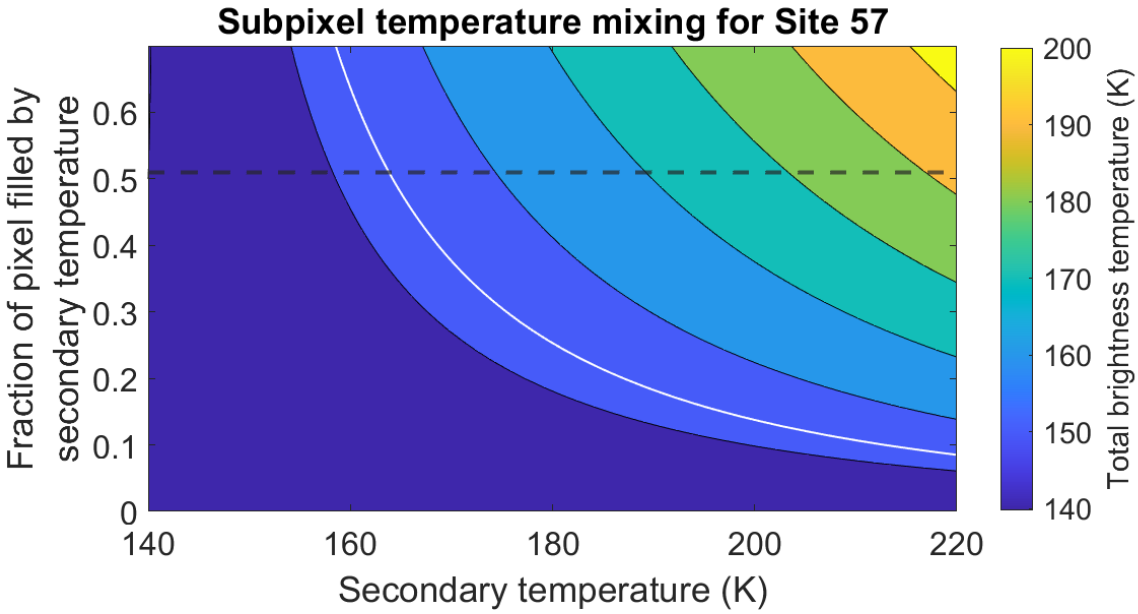

Figure 3.6: subpixel temperature mixing plot for site 57 with CO_2 ice temperature of 144.3 K. The same analysis as for Figure 3.5 applies. Site 57 had only one retrieval indicative of the presence of water ice, with a temperature of 164.19.

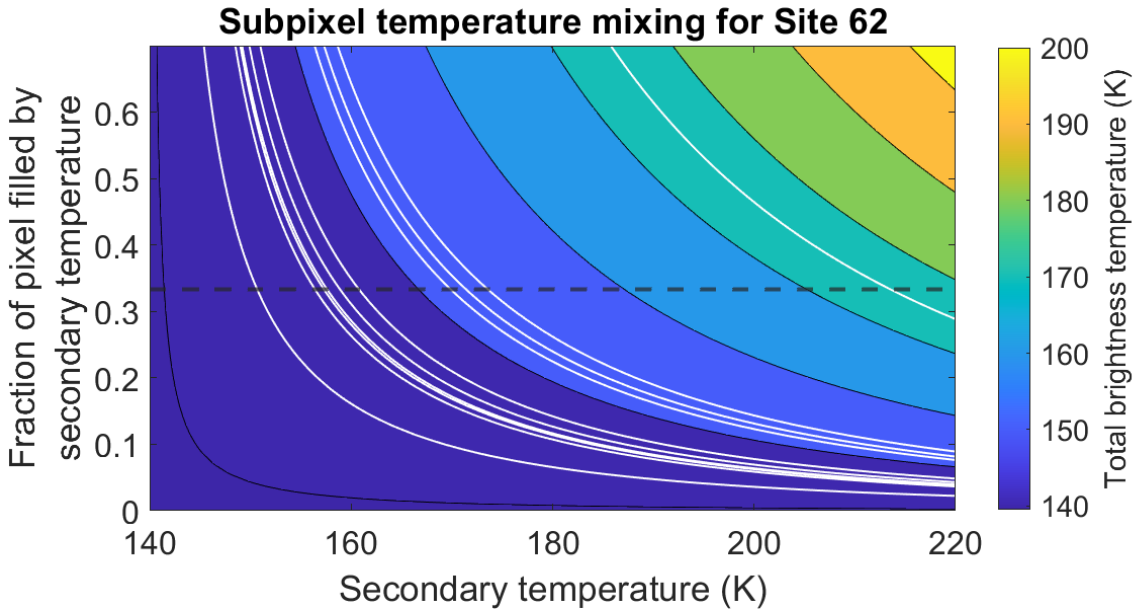

Figure 3.7: Subpixel temperature plot for site 62 with CO_2 ice temperature of 143.3 K. The same analysis as figure 3.5 applies. Site 62 had 10 retrievals indicative of water ice of which one was an outlier, the rest falling between 150-175 K.

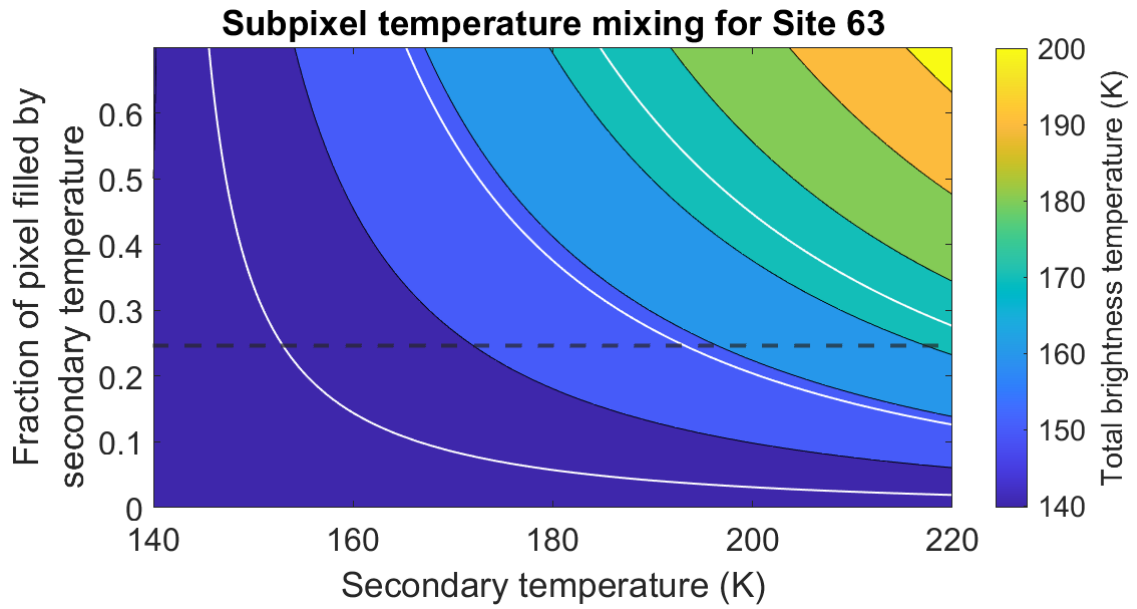

Figure 3.8: Subpixel temperature plot for site 63 with a CO_2 temperature of 144.3 K. Same analysis as Figure 3.5 applies. Site 63 had three retrievals indicative of water ice, two of which were outliers falling above 190 K, and the other being 154.16 K.

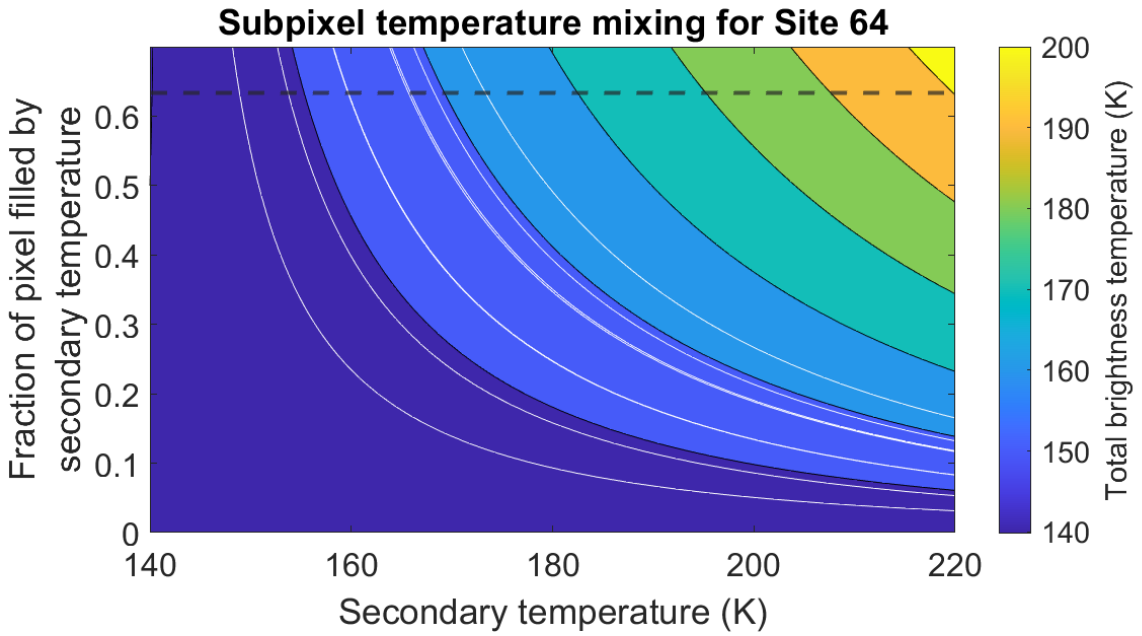

Figure 3.9: Subpixel temperature plot for Site 64 with a CO_2 ice temperature of 144.3 K. Same analysis as Figure 3.5 applies. Site 64 had 8 retrievals indicative of the presence of water ice, all of which fell within the typical range of 150-175 K.

The water-ice temperatures calculated for each data point are the lower bound water-ice temperature assuming that all area carved out by Swiss cheese features exposes water ice (shown in table 3.1). These temperatures range in L_s=255°-351° (late southern spring through summer) from MY 28 to 34. There does not appear to be any connection between solar longitude and water-ice temperature or any indication that years of global dust storms had any impact, although the 24 total retrievals are over 6 Martian years, making the data sparse. From the derived water-ice temperatures it is possible to calculate a mass loss rate using equation 3.5. These are also presented in Table 3.1.

Table 3.1 – Calculated water-ice temperatures and corresponding mass loss rates Swiss cheese sites.

Site ID	MY	L_s (°)	Water-ice Temperature (K)	Mass Loss Rate (kg/m^2s)
5	29	295.59	232.005	27.61×10^{-3}

5	32	285.07	215.907	3.98×10^{-3}
57	31	334.74	164.190	5.87×10^{-7}
62	28	329.68	158.162	1.44×10^{-7}
62	30	309.76	154.984	6.55×10^{-8}
62	30	328.43	157.840	1.33×10^{-7}
62	31	349.46	150.688	2.15×10^{-8}
62	31	300.13	155.553	7.55×10^{-8}
62	31	329.09	172.066	3.17×10^{-6}
62	32	310.79	169.177	1.74×10^{-6}
62	33	254.83	170.338	2.22×10^{-6}
62	34	328.21	156.399	9.33×10^{-8}
62	34	335.05	212.815	2.65×10^{-3}
63	32	347.08	154.164	5.32×10^{-8}
63	32	316.08	225.160	12.53×10^{-3}
63	33	292.02	193.429	1.54×10^{-4}
64	30	324.35	165.781	8.36×10^{-7}
64	31	306.26	168.260	1.43×10^{-6}
64	31	319.95	173.238	4.03×10^{-6}
64	31	332.02	165.478	7.82×10^{-7}
64	31	351.52	149.100	1.40×10^{-8}
64	34	284.67	153.794	4.84×10^{-8}
64	34	323.56	158.988	1.75×10^{-7}
64	34	330.97	159.687	2.07×10^{-7}

Excluding the water-ice temperatures greater than 200 K, there is an average water ice temperature of 160.94 K, which corresponds to a mass loss rate of 2.8×10^{-7} kg $m^{-2}s^{-1}$. Under the current configuration of Swiss cheese features and assuming that the total low standing area carved out by Swiss cheese (184.17 $km^{2)}$ is exposing water ice, and sublimating over the whole southern summer (154 sols), we have an upper limit on water vapour production of 7.01×10^{8} kg of water vapour, which mixed over all of Mars' atmosphere would produce 4.9×10^{-3} pr µm or a partial pressure of 1.8×10^{-5} Pa of water vapour.

Figure 3.10 shows the water vapour abundance produced over the range of derived water ice temperatures for the current configuration of Swiss cheese features, and it can be seen that changes in tens of Kelvin can result in large changes in the amount of water vapour produced. It is unlikely that the higher water ice temperatures are sustainable over large time periods, so looking at our nominal range of water-ice temperatures under current Swiss cheese conditions we see a maximum abundance of water vapour produced of 70.2×10^{-3} pr μm, which corresponds to a partial pressure of 2.6×10^{-4} Pa.

Taking an average MCS retrieved atmospheric temperature of 220 K for our points of interest, we computed the saturation vapour pressure for the southern summer atmosphere of 2.7 Pa. Since the partial pressures produced by Swiss cheese features are four to five orders of magnitude less than the SVP, the release of water vapour from Swiss cheese features alone will not cause the atmosphere to reach saturation, and our assumption of a dry atmosphere is a reasonable approximation in this case.

Both the average and maximum quantities of water vapour produced are extremely small compared to the average summer abundance seen in the southern hemisphere, so it is unlikely that the current configuration of Swiss cheese features contribute substantially to the overall atmospheric water vapour. In addition, this configuration could not have produced enough vapour to explain the 1969 observation.

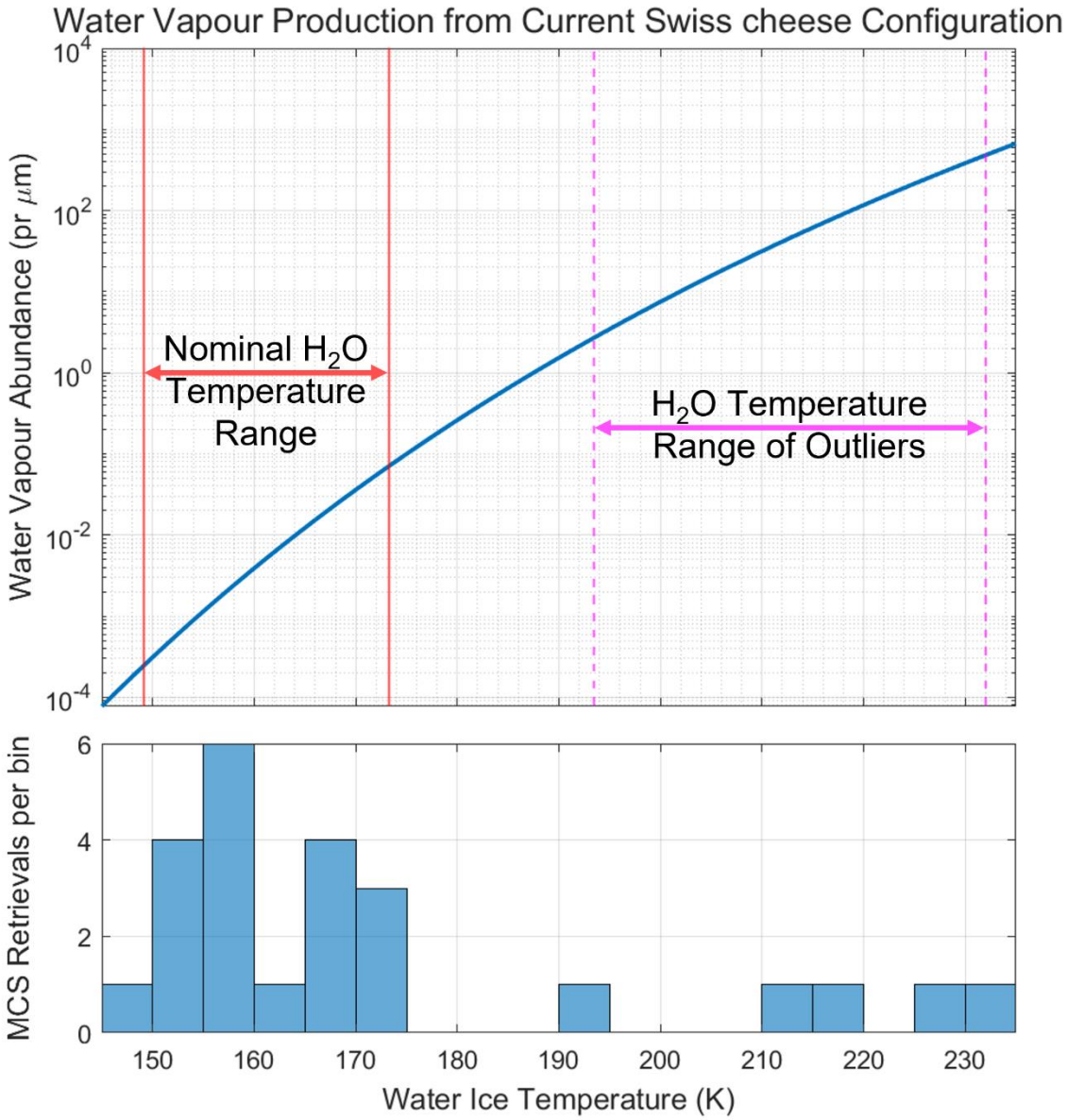

Figure 3.10: Water vapour production from the current configuration of Swiss cheese features. A histogram of derived MCS water ice temperature values shows a clustering of temperatures between 145 and 175 K, and the five outlier values.

While the current Swiss cheese extent does not have a large global effect on atmospheric water vapour, it begs the question of how extensive the Swiss cheese terrain would need to be to match the Barker et al (1970) observation. The 1969 observation saw a globally averaged abundance of 45 to 50 pr µm, about 2.5 times the average southern summer abundance of 20 pr µm (Trokhimovskiy et al, 2014).

Assuming that this nominal 20 pr µm of water vapour are already present in the southern summer, we were interested in seeing if we could sublimate the remaining 30 pr µm from Swiss cheese features alone. We assume the same sublimation period and similar surface temperatures as calculated for the present-day case. At a temperature of 173 K, the area of water-ice exposed by Swiss cheese features needs to increase by a factor of 427.2 to a total area of 78 678 km^2 or 91% of the total area of the SPRC. The lower limit of derived water-ice temperatures, 149 K, which produces $2.4x10^{-4}$ pr µm of water vapour, requires an increase of Swiss cheese area by a factor of $1.2x10^5$ or a total area of $2.3x10^7$ km^2, over 250 times the area of the SPRC. The sensitivity of vapour production to temperature suggests that a relatively minor (on order 10 K) warming of water ice could have a significant impact on the total vapour generated by Swiss cheese features, although methods leading to this warming are not known. However, if the outlier temperatures are reasonable representations of temperature that do occur for some fraction of exposed water ice, then it could be possible to get a higher sublimation rate at least for some part of the season.

We can conclude that higher temperature water ice could be responsible for the addition of 30 pr µm of water ice to the Martian atmosphere as a likely upper limit of reasonable vapour production, but temperatures closer to the lower end of our derived water-ice temperatures are not sufficient to produce that amount of water vapour from Swiss cheese terrain on the SPRC, given the magnitude of the area required.

3.3 Discussion

A lingering mystery of this work is the unusually high water-ice temperature observed. THEMIS observations of Swiss cheese terrain saw temperatures of around 160-190 K in the floors of Swiss cheese features (Byrne & Ingersoll, 2003), which agree with the majority of our calculated water-ice

temperatures. However, we saw five observations of water-ice temperatures predicted by our model outside this range, which correspond to unusually high brightness temperature retrievals (Table 3.2). The reason for these high retrievals is not understood.

Table 3.2: Unusually high water-ice temperatures, with retrieved brightness temperature and associated error, and calculated CO_2 frost temperatures.

Site ID	Scene Brightness Temperature (K)	Brightness Temperature Error (K)	CO_2 Frost Temperature (K)	Water-Ice Temperature (K)
5	186.278	0.042	145.801	215.906
5	197.903	0.038	146.140	232.005
62	174.888	0.043	144.320	212.815
63	158.548	0.049	143.847	237.288
63	174.155	0.044	144.134	222.457

The errors associated with the brightness temperature retrievals were all within the same range of values as the expected temperatures, and as described in Section 3.2, the cut off elevations of the retrievals do not indicate that they are unreliable or due to some instrumentation failure.

Another possible explanation for these retrievals is the presence of dust in the atmosphere. We looked at retrieved dust optical depths for site 62, the site with the greatest number of retrievals, and were unable to find any correlation between the dust opacity and retrieved surface temperature, as shown in Figure 3.11.

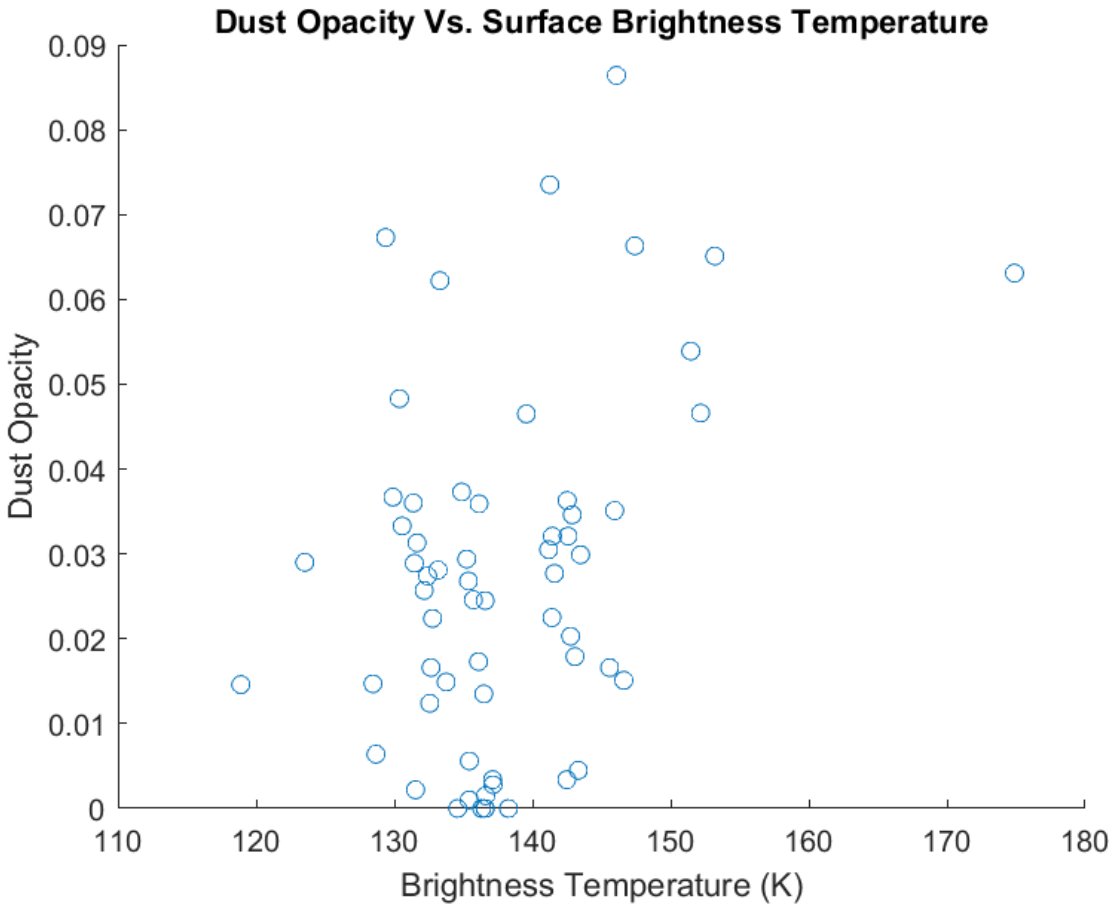

Figure 3.11: Dust optical Depth retrievals plotted against retrieved surface brightness temperature. There is no apparent correlation between the two variables.

Additionally, there did not seem to be a temporal component to these unusual retrievals. As can be seen in Figure 3.12, the retrievals associated with the unusual water-ice temperatures span 60° of L_s, out of the total range of ~100°. They also are not clustered in any particular Mars Year (as can be seen in Table 3.1). It is therefore unlikely that these high temperatures are associated with any global or regional dust storm.

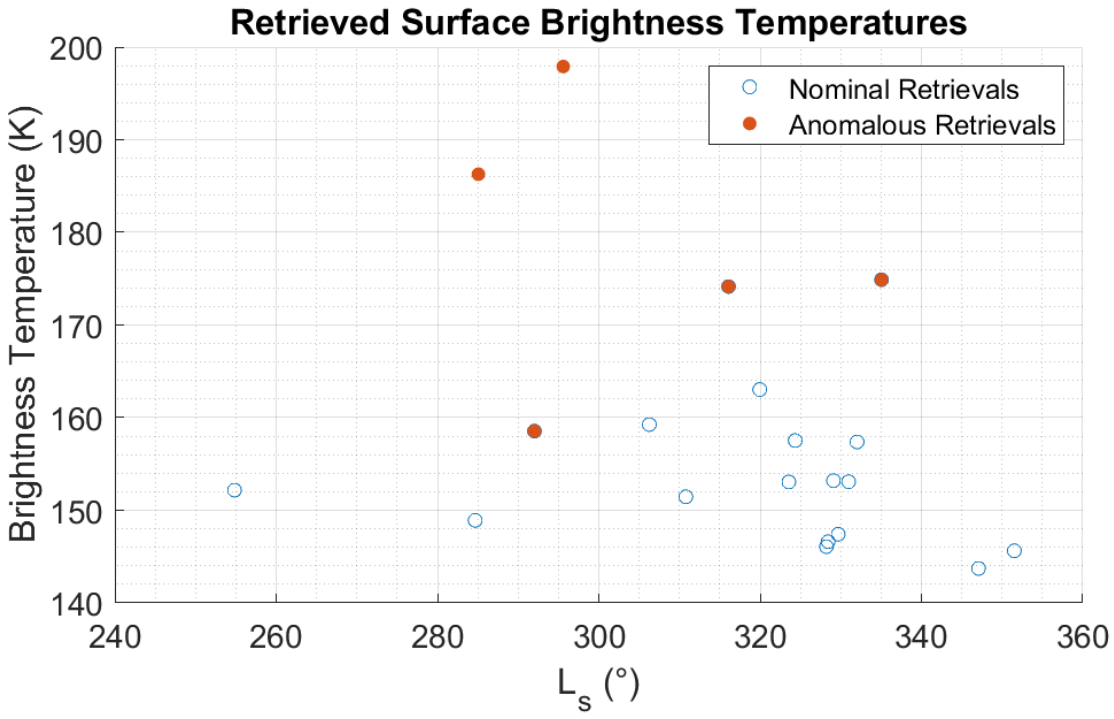

Figure 3.12: Retrieved surface brightness temperatures over the late southern spring/summer, over 6 Martian years. There are no obvious connections between the time of year and the brightness temperature.

If these temperatures do reflect actual water-ice temperatures at the SPRC surface, they require a massive temperature gradient between the exposed water ice and the surrounding CO_2 ice, and it is not likely that such a gradient is sustainable over any length of time. They would likely not sublimate at these temperatures for the entire summer season. As the MCS retrievals are only occasional, it is impossible to say how long these higher temperatures persist, and more regular retrievals of the sites would allow us to determine if they were transient or more permanent. However, it may be the case that slightly higher water-ice temperatures were also present in the 1969 Martian southern summer.

Given that much of the SPRC would need to be exposed water ice in order to sublimate 30 pr μm, there is also the possibility that there are latitudinal variations in temperature. We used the maximum expected temperature in our calculations in Section 3.2 over the entire SPRC, which covers around 5° of

latitude. This could lead to different sublimation rates at different locations on the SPRC, affecting the area required to sublimate 30 pr μm of water vapour. As can be seen in Figure 3.10, a small change in temperature can create a relatively large change in water vapour production, and so having areas of warmer water ice could produce more water vapour, necessitating a smaller total area to recreate the 1969 observation.

The sublimation model we use assumes complete sublimation into a dry atmosphere, with no recondensation of water vapour back onto the surface and ignoring any atmospheric influences such as wind. Our relatively simplistic sublimation model likely overestimates the water vapour production. Additionally, we use the same sublimation rate over the entire sol, not accounting for daytime or nighttime differences.

The partial pressure of 50 pr μm of water vapour is 0.19 Pa, which is still below our computed southern summer saturation vapour of 2.7 Pa, which supports our assumption of a dry atmosphere. This could indicate that a more complete model of the atmosphere would garner similar results to ours, and our sublimation rate is a fairly reasonable approximation.

While it is technically possible to recreate the 1969 observation by sublimating at 173 K from 78 678 km^2 of exposed water ice, because of the limitations on our sublimation model this does not definitively confirm the 1969 observation but does provide an upper limit on the amount of water vapour that could be derived from currently observed temperature conditions at the SPRC.

Finally, the relative lack of MCS observations of the mapped sites and the restrictions placed upon the retrievals such as proximity to troughs and minimum site size make it difficult to not only see temperature variations across the SPRC but also within a single site over years or over the course of a single season. Of the 24 observations of probable water ice, five were outliers, discussed earlier in this section, and they spanned six Martian years and nearly 100° of L_s. It is not possible to see whether there

is any interannual variation in water-ice temperature, or variation within the southern summer itself. We assumed in our calculations that water ice was exposed at a single temperature for the entirety of the southern summer, but having more retrievals over the season would allow us to see if the temperature varied and indeed if water ice was exposed for the whole season. If water ice is exposed for less time than our assumed 154 sols would mean that we would not be able to sublimate as much water vapour as we assume, and it may not be possible to recreate the 1969 observation from Swiss cheese feature sublimation alone.

These temperature retrievals also only encompass the recent past. MCS observations go back only to MY 29 (2007), so we are not able to know the variation in temperatures over the southern summer of 1969, and any temperature or range of temperatures we use in the sublimation calculation will be an estimation. Therefore, continued monitoring of Martian conditions is critical to continuing to evaluate these hypotheses about what effects the Martian climate over decadal time scales.

Chapter 4

Conclusions

4.1 Mars Year 35 Phase Function

The annual formation of the aphelion cloud belt is an important factor in the Martian water cycle, responsible for the asymmetry in distribution of water vapour (Wolff et al, 1999). Global dust storms can have a number of lasting impacts on the Martian climate, including truncating the ACB season. The work presented in Chapter 2 of this thesis was guided by determining of the GDS of MY 34 had any impact on the formation of aphelion water-ice clouds through study of the clouds' phase function and comparison of the MY 35 ACB phase function with that of the MY 34 ACB season, derived by Cooper et al (2019).

We used a total of 26 phase function sky survey observations from the Mars Science Laboratory, over the range of L_s=55°-160°, evenly divided between morning and afternoon observations. A mean phase function was derived from these observations covering scattering angles between 32°-155°, and was compared with the Cooper et al (2019) MY 34 mean phase function. We found that the two phase functions were very similar in shape, with the only major difference being the lack of a large maximum between ~35°-50° in our MY 35 phase function. The coefficient of determination (R^2=0.71) also indicated a fairly good fit between the two phase functions. This indicates that there were not any major impacts from the GDS on the dominant water-ice crystal geometry of the ACB clouds.

We also compared our MY 35 phase function with four water-ice cloud phase functions from orbiter observations (Clancy & Lee, 1991; Clancy et al, 2003) and found relatively poor fits with our phase function. There was some similarity in shape between the TES aphelion phase functions and our own, but not as close as the MY 34 phase function. The lack of agreement between these four phase functions and our MY 35 phase function likely has less to do with any changes in the scattering

properties of Mars water-ice clouds and more to do with the different methods used to derive these phase functions. Additionally, the wavelengths employed for both Viking IRTM and TES phase function determinations are significantly different than the NavCam's 600-850 nm bandpass. The solar band of the IRTM (0.3-3 μm) was used by Clancy & Lee (1991), and TES's solar and thermal infrared bands (0.3-3 μm and 5.8-50 μm, respectively) were used by Clancy et al (2003).

In order to attempt to constrain the water-ice crystal habit of the ACB clouds, we also compared our phase function to seven modeled water-ice crystal geometries. We again found that none of the phase functions fit particularly well with our mean phase function. This could be due to the fact that there is likely more than one single ice crystal shape present within the ACB clouds, as there is in earth-based water-ice clouds (Whiteway et al, 2004). It is also likely that the water-ice crystal shapes created under Martian conditions are different to those produced in Earth's atmosphere.

Finally, we compared the mean phase functions of morning and afternoon clouds, as previous studies have found differences in optical depth (Kloos et al, 2018) and altitude (Campbell et al, 2019) in clouds observed at different times of day. Despite this, we did not see any significant differences in the mean curves of the morning or afternoon phase functions, indicating the ice crystal species are likely the same in morning and afternoon clouds.

The main point at which both the MY 35 phase function and the MY 34 phase function do not behave as expected is at lower scattering angles, <60°. We expect to see an increase in phase function magnitude as we approach forward scattering, which is absent from both curves, especially the MY 35 curve. This is potentially an indication that the curves are not accurate. The 95% confidence intervals of both curves also increase at lower scattering angles. Frames closer to the sun, as described in Section 2.2, are more likely to have artifacts in them making the detection of clouds difficult, which could be a potential reason for the behaviour of the curve closer to forward scattering angles.

Future work to answer some of the remaining questions and improve the results is presented in Chapter 5.

4.2 Atmospheric Water Vapour Contributions from Swiss Cheese Terrain

The Martian poles are the largest reservoirs of water on Mars. The yearly cycle of sublimation and transport between the poles has important impacts on Mars' climate. Typically, only around 20 pr µm is produced during the southern summer. However, in 1969 (MY 8) between 45 and 50 pr µm of water vapour were detected by earth-based telescopes (Barker et al, 1970). The aim of this work was the determine an upper bound on current water vapour contributions from the Swiss cheese features of the SPRC and to use these constraints to determine what are of Swiss cheese terrain would be required to replicate the 1969 observation. If that area was much greater than the total area of the SPRC under our upper limit assumptions, the contribution of water ice exposed by Swiss cheese features can be ruled out as a feasible source of vapour in the 1969 observation. If not, Swiss cheese terrain could plausibly be an important source of additional atmospheric water vapour.

We mapped the current configuration of Swiss cheese features, which account for around 0.2% of the total area of the SPRC at present. MCS temperature retrievals of Swiss cheese sites were indicative of the presence of water ice in late southern spring and summer. We determined an upper limit on water vapour sublimation from the current configuration of Swiss cheese features, assuming the entire mapped area of pits exposes water ice which sublimated throughout the southern summer season and found that the globally averaged water vapour abundance produced (at maximum, 70.2×10^{-3} pr µm) is not enough to have an appreciable impact on atmospheric water vapour.

In order to bring this maximum vapour production up to levels seen in the 1969 observation, the area of water ice exposed by Swiss cheese needs to increase to 91% of the total area of the SPRC. It is

impossible to create the required water vapour from Swiss cheese features alone at lower temperatures.

Chapter 5

Future Work

5.1 Mars Year 35 Phase Function

As mentioned in Section 4.1, the wavelengths used to capture phase function information from Viking IRTM and TES are different from those used in the MSL NavCams, making comparing the phase functions problematic. Future work could look at finding a particle model that matches both phase functions at the varying wavelengths, which would help to further constrain the dominant water-ice crystal shape in Martian water-ice clouds.

In addition, further investigation into the discrepancy between the behaviour of the MY 34/35 phase functions at low scattering angles and the expected behaviour of water-ice crystals in the forward scattering region is needed, as well as looking at whether or not the mean phase function curves accurately represent the scattering occurring in ACB clouds. It could be that it is not possible to resolve this, as we are not able to observe clouds close to the sun, however if it could be determined that there is a computational reason for the apparent decrease in magnitude at low scattering angles, this could also help produce a better mean curve.

Using different optical depth values may also improve the phase function calculation. The limitations of the MCS water-ice opacities are discussed in section 2.3. Being able to use opacity values of the actual clouds we are observing versus an average value over 10° of L_s would allow us to create a phase function more finely attuned to the individual clouds seen in the PFSS. In addition, distinguishing between morning and afternoon clouds could shed light on if there are in fact differences in their dominant geometries that are being lost by using a mean optical depth value.

The phase function calculation could be further improved by increasing the number of data points from which the mean curve is calculated. As the NavCam FOV is 45°, each pointing includes a number of scattering angles, but only one point is selected from each movie at this point. Each movie could be divided into quadrants, allowing the selection of multiple points within a single frame. Additionally, the current method is to calculate a mean phase function for all observations together (or divided into morning and afternoon, but still spanning the entire ACB season). If individual phase functions could be calculated for each observation, this could indicate any changes over the course of the ACB season, more than 100° of solar longitude. Further extending the dataset by continuing to derive the phase function for future Mars years can help to determine if any interannual variation exists, especially moving away from the MY 34 GDS.

5.2 Atmospheric Water Vapour Contributions from Swiss Cheese Terrain

In order to better understand our calculated water-ice temperatures, Thermal Emission Imaging System (THEMIS) temperature retrievals could be used. THEMIS has a resolution of 100 m/pixel (Christensen et al, 2004), on the order of larger Swiss cheese features. This could provide more temperature retrievals at a finer resolution, and perhaps determine if the anomalous temperatures of greater than 190 K are repeatable. Using THEMIS would also allow us to examine sites that fell below the minimum area for MCS retrievals, but this is left to future work as part of refining the overall estimates of current and historical water vapour production.

In addition, our sublimation calculation assumes a dry atmosphere and instantaneous sublimation from exposed water ice into the atmosphere with no recondensation back onto the surface. A more sophisticated sublimation model could further constrain the amount of water vapour released from the

current configuration of Swiss cheese features and provide more narrow constraints on what conditions would be required to recreate the 1969 observation through exposure of water ice on the SPRC.

Works Cited

Aoki, S., Vandaele, A. C., Daerden, F., Villanueva, G. L., Liuzzi, G., Thomas, I. R., Erwin, J. T., Trompet, L., Robert, S., Neary, L., Viscardy, S., Clancy, R. T., Smith, M. D., Lopez-Valverde, M. A., Hill, B., Ristic, B., Patel, M. R., Bellucci, G., & Lopez-Moreno, J. -J. (2019). Water Vapor Vertical Profiles on Mars in Dust Storms Observed by TGO/NOMAD. *Journal of Geophysical Research: Planets*, *124*(12), 3482–3497. https://doi.org/10.1029/2019je006109

Barker, E. S., Schorn, R. A., Woszczyk, A., Tull, R. G., & Little, S. J. (1970). Mars: Detection of Atmospheric Water Vapor during the Southern Hemisphere Spring and Summer Season. *Science*, *170*(3964), 1308–1310. https://doi.org/10.1126/science.170.3964.1308

Buhler, P. B., Ingersoll, A. P., Ehlmann, B. L., Fassett, C. I., & Head, J. W. (2017). How the martian residual south polar cap develops quasi-circular and heart-shaped pits, troughs, and moats. *Icarus*, *286*, 69–93. https://doi.org/10.1016/j.icarus.2017.01.012

Byrne, S., & Ingersoll, A. P. (2003). A Sublimation Model for Martian South Polar Ice Features. *Science*, *299*(5609), 1051–1053. https://doi.org/10.1126/science.1080148

Byrne, S. (2009). The Polar Deposits of Mars. *Annual Review of Earth and Planetary Sciences*, *37*(1), 535–560. https://doi.org/10.1146/annurev.earth.031208.100101

Byrne, S., Hayne, P. O., Becerra, P., & HiRISE Team. (2015). Evolution and Stability of the Residual CO2 Ice Cap. *46th Lunar and Planetary Science Conference*, 1657.

Campbell, C. L., Kling, A. M., Guzewich, S. D., Smith, C. L., Kloos, J. L., Lemmon, M. T., Moore, C. A., Cooper, B. A., Haberle, R. M., & Moores, J. E. (2020). Estimating the altitudes of Martian water-ice clouds above the Mars Science Laboratory rover landing site. *Planetary and Space Science*, *182*, 104785. https://doi.org/10.1016/j.pss.2019.104785

Campbell, C. L., Meka, S., Marrable, D., Rohl, A. L., Chai, K., Benedix, G. K., Smith, C. L., & Moores, J. E. (2021). A self-supervised learning based approach to analyze Martian water–ice cloud properties for planetary atmospheric applications. *Acta Astronautica*, *181*, 1–13. https://doi.org/10.1016/j.actaastro.2020.12.041

Cantor, B. A. (2007). MOC observations of the 2001 Mars planet-encircling dust storm. *Icarus*, *186*(1), 60–96. https://doi.org/10.1016/j.icarus.2006.08.019

Cartwright, S. F. A., Seelos, F. P., Poffenbarger, R. T., & Calvin, W. M. (2021). Creating Multispectal Mosaics Of Mars' South Polar Residual Cap From CRISM Mapping Data. *51st Lunar and Planetary Science Conference*. Lunar and Planetary Science Conference.

Chepfer, H., Minnis, P., Young, D., Nguyen, L., & Arduini, R. F. (2002). Estimation of cirrus cloud effective ice crystal shapes using visible reflectances from dual-satellite measurements. *Journal of Geophysical Research: Atmospheres*, *107*(D23), AAC 21-1-AAC 21-16. https://doi.org/10.1029/2000JD000240

Christensen, P. R., Jakosky, B. M., Kieffer, H. H., Malin, M. C., McSween, Jr., H. Y., Nealson, K., Mehall, G. L., Silverman, S. H., Ferry, S., Caplinger, M., & Ravine, M. (2004). The Thermal Emission Imaging System (THEMIS) for the Mars 2001 Odyssey Mission. *Space Science Reviews*, *110*(1/2), 85–130. https://doi.org/10.1023/B:SPAC.0000021008.16305.94

Clancy, R. T., & Lee, S. W. (1991). A new look at dust and clouds in the Mars atmosphere: Analysis of emission-phase-function sequences from global viking IRTM observations. *Icarus*, *93*(1), 135–158. https://doi.org/10.1016/0019-1035(91)90169-T

Clancy, R. T., Grossman, A. W., Wolff, M. J., James, P. B., Rudy, D. J., Billawala, Y. N., Sandor, B. J., Lee, S. W., & Muhleman, D. O. (1996). Water Vapor Saturation at Low Altitudes around Mars Aphelion: A Key to Mars Climate? *Icarus*, *122*(1), 36–62. https://doi.org/10.1006/icar.1996.0108

Clancy, R. T., Sandor, B. J., Wolff, M. J., Christensen, P. R., Smith, M. D., Pearl, J. C., Conrath, B. J., & Wilson, R. J. (2000). An intercomparison of ground-based millimeter, MGS TES, and Viking atmospheric temperature measurements: Seasonal and interannual variability of temperatures and dust loading in the global Mars atmosphere. *Journal of Geophysical Research: Planets*, *105*(E4), 9553–9571. https://doi.org/10.1029/1999JE001089

Clancy, R. T., Wolff, M. J., & Christensen, P. R. (2003). Mars aerosol studies with the MGS TES emission phase function observations: Optical depths, particle sizes, and ice cloud types versus latitude and solar longitude. *Journal of Geophysical Research*, *108*(E9), 5098. https://doi.org/10.1029/2003JE002058

Clancy, R. T., Montmessin, F., Benson, J., Daerden, F., Colaprete, A., & Wolff, M. J. (2017). Mars Clouds. In R. M. Haberle, R. T. Clancy, F. Forget, M. D. Smith, & R. W. Zurek (Eds.), *The Atmosphere and Climate of Mars* (pp. 76–105). Cambridge University Press. https://doi.org/10.1017/9781139060172.005

Cooper, B. A., Moores, J. E., Ellison, D. J., Kloos, J. L., Smith, C. L., Guzewich, S. D., & Campbell, C. L. (2019). Constraints on Mars Aphelion Cloud Belt phase function and ice crystal geometries. *Planetary and Space Science*, *168*, 62–72. https://doi.org/10.1016/j.pss.2019.01.005

Dickson, J. L., Kerber, L. A., Fassett, C. I., & Ehlmann, B. L. (2018). A Global, Blended CTX Mosaic of Mars with Vectorized Seam Mapping: A New Mosaicking Pipeline Using Principles of Non-Destructive Image Editing. *49th Lunar and Planetary Science Conference*. Lunar and Planetary Science Conference.

Grotzinger, J. P., Crisp, J., Vasavada, A. R., Anderson, R. C., Baker, C. J., Barry, R., Blake, D. F., Conrad, P., Edgett, K. S., Ferdowski, B., Gellert, R., Gilbert, J. B., Golombek, M., Gómez-Elvira, J., Hassler, D. M., Jandura, L., Litvak, M., Mahaffy, P., Maki, J., … Wiens, R. C. (2012). Mars Science Laboratory Mission and Science Investigation. *Space Science Reviews*, *170*(1–4), 5–56. https://doi.org/10.1007/s11214-012-9892-2

Guzewich, S. D., Lemmon, M., Smith, C. L., Martínez, G., Vicente-Retortillo, Á., Newman, C. E., Baker, M., Campbell, C., Cooper, B., Gómez-Elvira, J., Harri, A. -M., Hassler, D., Martin-Torres, F. J., Mcconnochie, T., Moores, J. E., Kahanpää, H., Khayat, A., Richardson, M. I., Smith, M. D., … Zorzano Mier, M. (2019). Mars Science Laboratory Observations of the 2018/Mars Year 34 Global Dust Storm. *Geophysical Research Letters*, *46*(1), 71–79. https://doi.org/10.1029/2018gl080839

Guzewich, S. D., Wilson, R. J., McConnochie, T. H., Toigo, A. D., Banfield, D. J., & Smith, M. D. (2014). Thermal tides during the 2001 Martian global-scale dust storm. *Journal of Geophysical Research: Planets*, *119*(3), 506–519. https://doi.org/10.1002/2013JE004502

Hayne, P. O., Paige, D. A., Schofield, J. T., Kass, D. M., Kleinböhl, A., Heavens, N. G., & McCleese, D. J. (2012). Carbon dioxide snow clouds on Mars: South polar winter observations by the Mars Climate Sounder: POLAR SNOW CLOUDS ON MARS. *Journal of Geophysical Research: Planets*, *117*(E8). https://doi.org/10.1029/2011JE004040

Heavens, N. G., Kleinböhl, A., Chaffin, M. S., Halekas, J. S., Kass, D. M., Hayne, P. O., McCleese, D. J., Piqueux, S., Shirley, J. H., & Schofield, J. T. (2018). Hydrogen escape from Mars enhanced by deep convection in dust storms. *Nature Astronomy*, *2*(2), 126–132. https://doi.org/10.1038/s41550-017-0353-4

Herschel, W. (1784). On the Remarkable Appearances at the Polar Regions of the Planet Mars, the Inclination of Its Axis, the Position of Its Poles, and Its Spheroidical Figure; With a Few Hints Relating to Its Real Diameter and Atmosphere. By William Herschel, Esq. F. R. S. *Philosophical Transactions of the Royal Society of London*, *74*, 233–273.

Jakosky, B. M., & Barker, E. S. (1984). Comparison of ground-based and Viking Orbiter measurements of Martian water vapor: Variability of the seasonal cycle. *Icarus*, *57*(3), 322–334. https://doi.org/10.1016/0019-1035(84)90121-0

James, P. B., Kieffer, H. H., & Paige, D. A. (1992). The seasonal cycle of carbon dioxide on Mars. In H. H. Kieffer (Ed.), *Mars* (pp. 934–968).

Kahre, M. A., Murphy, J. R., Newman, C. E., Wilson, R. J., Cantor, B. A., Lemmon, M. T., & Wolff, M. J. (2017). The Mars Dust Cycle. In R. M. Haberle, R. T. Clancy, F. Forget, M. D. Smith, & R. W. Zurek (Eds.), *The Atmosphere and Climate of Mars* (pp. 295–337). Cambridge University Press. https://doi.org/10.1017/9781139060172.010

Kleinböhl, A., Schofield, J. T., Kass, D. M., Abdou, W. A., Backus, C. R., Sen, B., Shirley, J. H., Lawson, W. G., Richardson, M. I., Taylor, F. W., Teanby, N. A., & McCleese, D. J. (2009). Mars Climate Sounder limb profile retrieval of atmospheric temperature, pressure, and dust and water ice opacity: MCS RETRIEVALS. *Journal of Geophysical Research: Planets*, *114*(E10), n/a-n/a. https://doi.org/10.1029/2009JE003358

Kloos, J. L., Moores, J. E., Lemmon, M., Kass, D., Francis, R., de la Torre Juárez, M., Zorzano, M.-P., & Martín-Torres, F. J. (2016). The first Martian year of cloud activity from Mars Science Laboratory (sol 0–800). *Advances in Space Research*, *57*(5), 1223–1240. https://doi.org/10.1016/j.asr.2015.12.040

Kloos, J. L., Moores, J. E., Whiteway, J. A., & Aggarwal, M. (2018). Interannual and Diurnal Variability in Water Ice Clouds Observed from MSL Over Two Martian Years. *Journal of Geophysical Research: Planets*, *123*(1), 233–245. https://doi.org/10.1002/2017JE005314

Lemmon, M. T., Wolff, M. J., Bell, J. F., Smith, M. D., Cantor, B. A., & Smith, P. H. (2015). Dust aerosol, clouds, and the atmospheric optical depth record over 5 Mars years of the Mars Exploration Rover mission. *Icarus*, *251*, 96–111. https://doi.org/10.1016/j.icarus.2014.03.029

Lemmon, M. T., Guzewich, S. D., McConnochie, T., Vicente-Retortillo, A., Martínez, G., Smith, M. D., Bell, J. F., Wellington, D., & Jacob, S. (2019). Large Dust Aerosol Sizes Seen During the 2018 Martian Global Dust Event by the Curiosity Rover. *Geophysical Research Letters*, *46*(16), 9448–9456. https://doi.org/10.1029/2019GL084407

Liou, K.-N. (2002). *An introduction to atmospheric radiation* (2nd ed). Academic Press.

Maki, J., Thiessen, D., Pourangi, A., Kobzeff, P., Litwin, T., Scherr, L., Elliott, S., Dingizian, A., & Maimone, M. (2012). The Mars Science Laboratory Engineering Cameras. *Space Science Reviews*, *170*(1–4), 77–93. https://doi.org/10.1007/s11214-012-9882-4

Malin, M. C., Bell, J. F., Cantor, B. A., Caplinger, M. A., Calvin, W. M., Clancy, R. T., Edgett, K. S., Edwards, L., Haberle, R. M., James, P. B., Lee, S. W., Ravine, M. A., Thomas, P. C., & Wolff, M. J. (2007). Context Camera Investigation on board the Mars Reconnaissance Orbiter. *Journal of Geophysical Research*, *112*(E5), E05S04. https://doi.org/10.1029/2006JE002808

Marti, J., & Mauersberger, K. (1993). A survey and new measurements of ice vapor pressure at temperatures between 170 and 250K. *Geophysical Research Letters*, *20*(5), 363–366. https://doi.org/10.1029/93GL00105

McCleese, D. J., Schofield, J. T., Taylor, F. W., Calcutt, S. B., Foote, M. C., Kass, D. M., Leovy, C. B., Paige, D. A., Read, P. L., & Zurek, R. W. (2007). Mars Climate Sounder: An investigation of thermal and water vapor structure, dust and condensate distributions in the atmosphere, and energy balance of the polar regions. *Journal of Geophysical Research*, *112*(E5), E05S06. https://doi.org/10.1029/2006JE002790

Montmessin, F., Smith, M. D., Langevin, Y., Mellon, M. T., & Fedorova, A. (2017). The Water Cycle. In R. M. Haberle, R. T. Clancy, F. Forget, M. D. Smith, & R. W. Zurek (Eds.), *The Atmosphere and Climate of Mars* (pp. 338–373). Cambridge University Press. https://doi.org/10.1017/9781139060172.011

Moores, J. E., Lemmon, M. T., Rafkin, S. C. R., Francis, R., Pla-Garcia, J., De La Torre Juárez, M., Bean, K., Kass, D., Haberle, R., Newman, C., Mischna, M., Vasavada, A., Rennó, N., Bell, J., Calef, F., Cantor, B., Mcconnochie, T. H., Harri, A.-M., Genzer, M., … Mccullough, E. (2015). Atmospheric movies

acquired at the Mars Science Laboratory landing site: Cloud morphology, frequency and significance to the Gale Crater water cycle and Phoenix mission results. *Advances in Space Research*, *55*(9), 2217–2238. https://doi.org/10.1016/j.asr.2015.02.007

Phillips, R. J., Davis, B. J., Tanaka, K. L., Byrne, S., Mellon, M. T., Putzig, N. E., Haberle, R. M., Kahre, M. A., Campbell, B. A., Carter, L. M., Smith, I. B., Holt, J. W., Smrekar, S. E., Nunes, D. C., Plaut, J. J., Egan, A. F., Titus, T. N., & Seu, R. (2011). Massive CO2 Ice Deposits Sequestered in the South Polar Layered Deposits of Mars. *Science*. https://www.science.org/doi/abs/10.1126/science.1203091

Schorghofer, N. (2008). The Lifetime of Ice on Main Belt Asteroids. *The Astrophysical Journal*, *682*(1), 697. https://doi.org/10.1086/588633

Smith, M. D. (2002). The annual cycle of water vapor on Mars as observed by the Thermal Emission Spectrometer. *Journal of Geophysical Research: Planets*, *107*(E11), 25-1-25–19. https://doi.org/10.1029/2001JE001522

Smith, M. D. (2004). Interannual variability in TES atmospheric observations of Mars during 1999–2003. *Icarus*, *167*(1), 148–165. https://doi.org/10.1016/j.icarus.2003.09.010

Spinrad, H., Münch, G., & Kaplan, L. D. (1963). Letter to the Editor: The Detection of Water Vapor on Mars. *The Astrophysical Journal*, *137*, 1319. https://doi.org/10.1086/147613

Stcherbinine, A., Vincendon, M., Montmessin, F., Wolff, M. J., Korablev, O., Fedorova, A., Trokhimovskiy, A., Patrakeev, A., Lacombe, G., Baggio, L., & Shakun, A. (2020). Martian Water Ice Clouds During the 2018 Global Dust Storm as Observed by the ACS-MIR Channel Onboard the Trace Gas Orbiter. *Journal of Geophysical Research: Planets*, *125*(3). https://doi.org/10.1029/2019JE006300

Tamppari, L. K., Zurek, R. W., & Paige, D. A. (2003). Viking-era diurnal water-ice clouds. *Journal of Geophysical Research: Planets*, *108*(E7). https://doi.org/10.1029/2002JE001911

Tanaka, K. L., & Scott, D. H. (1999). *Mars Geologic Map of the Polar Regions* [Map]. 1:15 000 000, USGS Astrogeology Science Center.

Thomas, P. C., James, P. B., Calvin, W. M., Haberle, R., & Malin, M. C. (2009). Residual south polar cap of Mars: Stratigraphy, history, and implications of recent changes. *Icarus*, *203*(2), 352–375. https://doi.org/10.1016/j.icarus.2009.05.014

Tomasko, M. G., Doose, L. R., Lemmon, M., Smith, P. H., & Wegryn, E. (1999). Properties of dust in the Martian atmosphere from the Imager on Mars Pathfinder. *Journal of Geophysical Research: Planets*, *104*(E4), 8987–9007. https://doi.org/10.1029/1998JE900016

Trokhimovskiy, A., Fedorova, A., Korablev, O., Montmessin, F., Bertaux, J.-L., Rodin, A., & Smith, M. D. (2015). Mars' water vapor mapping by the SPICAM IR spectrometer: Five martian years of observations. *Icarus*, *251*, 50–64. https://doi.org/10.1016/j.icarus.2014.10.007

Wang, C., Yang, P., Dessler, A., Baum, B. A., & Hu, Y. (2014). Estimation of the cirrus cloud scattering phase function from satellite observations. *Journal of Quantitative Spectroscopy and Radiative Transfer*, *138*, 36–49. https://doi.org/10.1016/j.jqsrt.2014.02.001

Warren, S. G., Wiscombe, W. J., & Firestone, J. F. (1990). Spectral albedo and emissivity of CO2 in Martian polar caps: Model results. *Journal of Geophysical Research*, *95*(B9), 14717. https://doi.org/10.1029/JB095iB09p14717

Whiteway, J., Cook, C., Gallagher, M., Choularton, T., Harries, J., Connolly, P., Busen, R., Bower, K., Flynn, M., May, P., Aspey, R., & Hacker, J. (2004). Anatomy of cirrus clouds: Results from the Emerald airborne campaigns. *Geophysical Research Letters*, *31*(24). https://doi.org/10.1029/2004GL021201

Williams, D. R. (2020). *Mars Fact Sheet*. NASA Space Science Data Coordinated Archive. https://nssdc.gsfc.nasa.gov/planetary/factsheet/marsfact.html

Wolff, M. J., Bell, J. F., James, P. B., Clancy, R. T., & Lee, S. W. (1999). Hubble Space Telescope observations of the Martian aphelion cloud belt prior to the Pathfinder mission: Seasonal and interannual variations. *Journal of Geophysical Research: Planets*, *104*(E4), 9027–9041. https://doi.org/10.1029/98je01967

Wolkenberg, P., Giuranna, M., M., Grassi, D., & Amoroso, M. (2020). Similarities and Differences of Global Dust Storms in MY 25, 28, and 34. *Journal of Geophysical Research: Planets*, *125*(3). https://doi.org/10.1029/2019je006104

Whiteway, J., Cook, C., Gallagher, M., Choularton, T., Harries, J., Connolly, P., Busen, R., Bower, K., Flynn, M., May, P., Aspey, R., & Hacker, J. (2004). Anatomy of cirrus clouds: Results from the

Emerald airborne campaigns. *Geophysical Research Letters*, *31*(24). https://doi.org/10.1029/2004GL021201

Yang, P., Baum, B. A., Heymsfield, A. J., Hu, Y. X., Huang, H.-L., Tsay, S.-C., & Ackerman, S. (2003). Single-scattering properties of droxtals. *Journal of Quantitative Spectroscopy and Radiative Transfer*, *79–80*, 1159–1169. https://doi.org/10.1016/S0022-4073(02)00347-3

Yang, P., & Liou, K. N. (1996). Geometric-optics–integral-equation method for light scattering by nonspherical ice crystals. *Applied Optics*, *35*(33), 6568. https://doi.org/10.1364/AO.35.006568

Appendix A

Mapped Swiss Cheese Area

Table A.1 – Mapped areas of Swiss cheese features and percent carved out in each Swiss cheese terrain site. Areas that were rejected for mapping and indicated with a dash.

Site ID	Total Site Area (km^2)	Swiss Cheese Feature Area (km^2)	% Mapped	% Carved Out
0	16.847	2.482	25	58.923
1	18.699	2.039	25	43.625
2	18.574	1.731	25	37.278
3	2.796	1.217	100	43.534
4	6.753	3.215	100	47.617
5	55.819	6.390	25	45.789
6	72.304	7.296	25	40.361
7	2.360	0.783	100	33.154
8	60.017	7.627	25	50.830
9	56.704	5.928	25	41.814
10	6.100	3.228	100	52.920
11	26.930	2.415	25	35.868
12	19.036	1.081	25	22.723
13	1.354	1.044	100	77.087
14	2.048	0.921	100	44.995
15	7.007	4.590	100	65.503
16	2.388	-	-	-
17	1.246	0.776	100	62.297
18	2.697	1.483	100	54.964
19	14.242	1.445	25	40.597
20	33.186	3.565	25	42.971
21	41.744	4.772	25	45.730
22	1.445	0.729	100	50.451

23	1.633	0.546	100	33.456
24	2.014	0.993	100	49.326
25	5.442	-	-	-
26	13.567	0.392	25	11.545
27	0.830	0.534	100	64.266
28	2.430	0.726	100	29.881
29	26.848	2.975	25	44.324
30	12.001	1.404	25	46.794
31	3.558	1.730	100	48.621
32	18.522	1.620	25	34.979
33	6.798	3.544	100	52.129
34	53.260	3.168	25	23.790
35	2.051	0.893	100	43.529
36	6.896	3.172	100	45.994
37	1.410	0.705	100	50.021
38	35.206	2.638	25	29.972
39	1.077	0.310	100	28.812
40	9.803	6.593	100	67.250
42	4.742	2.967	100	62.558
44	2.315	0.947	100	40.917
45	1.106	0.278	100	25.136
47	0.793	0.582	100	73.372
48	1.075	0.597	100	55.538
49	0.995	0.846	100	84.991
50	0.670	0.377	100	56.230
51	34.450	4.362	25	50.650
52	9.561	4.628	100	48.409
53	14.697	1.968	25	53.556
54	4.945	2.218	100	44.854
55	23.250	1.760	25	30.274
56	7.404	3.970	100	53.621

57	21.816	2.782	25	51.009
58	55.890	3.294	25	23.575
59	13.351	1.104	25	33.062
60	3.024	0.575	100	19.011
61	4.904	-	-	-
62	472.239	21.282	16.6	27.148
63	29.894	1.843	25	24.666
64	37.739	5.972	25	63.293
65	3.794	0.529	100	13.936
66	28.164	2.105	25	29.892
67	2.963	1.436	100	48.456
68	1.962	0.712	100	36.278
69	17.536	1.407	25	32.096
70	2.205	0.516	100	23.418
71	2.120	0.557	100	26.266
72	0.679	0.264	100	38.827
73	3.185	1.585	100	49.772
74	4.254	1.598	100	37.578
75	1.939	0.925	100	47.681
76	0.782	0.368	100	46.986
77	1.182	0.524	100	44.322
79	1.648	0.478	100	29.007
80	1.039	0.236	100	22.661
81	1.202	0.475	100	39.535
82	6.444	-	-	-
83	5.821	2.499	100	42.929
85	21.639	2.202	25	40.701
86	3.603	1.738	100	48.221
87	97.165	4.974	25	20.477